



## Supplementary Materials for

### **Determination of in vivo target search kinetics of regulatory noncoding RNA**

Jingyi Fei, Digvijay Singh, Qiucen Zhang, Seongjin Park, Divya Balasubramanian,  
Ido Golding, Carin K. Vanderpool,\* Taekjip Ha\*

\*Corresponding author. E-mail: tjha@illinois.edu (T.H.); cvanderp@life.uiuc.edu (C.K.V.)

Published 20 March 2015, *Science* **347**, 1371 (2015)  
DOI: 10.1126/science.1258849

#### **This PDF file includes:**

Materials and Methods  
Supplementary Text  
Figs. S1 to S18  
Tables S1 to S5  
References

**Other Supplementary Material for this manuscript includes the following:**  
(available at [www.sciencemag.org/cgi/content/full/347/6228/1371/DC1](http://www.sciencemag.org/cgi/content/full/347/6228/1371/DC1))

Movies S1 to S3

## Materials and Methods

### 1.1 Bacterial strain construction

The strain CS196, (*ptsG::tet*) knockout strain, was created using lambda red recombination as described earlier (30) using primers O-CS244 (CCCCC CTTGC CACGC GTGAG AACGT AAAAA AAGCA CCCAT ACTAG ACATC ATTAA TTCCT) and O-CS245 (GAAAC CGTAA ATGCC AAACG CAACT ACCGG GTTCT GGTA GAAGC TAAAT CTTCT TTATC).

### 1.2 Growth of cultures for time-course measurements, fixation and permeabilization

For all experiments on SgrS, bacterial strains were grown overnight in MOPS EZ rich defined medium (TEKnova) supplemented with 0.2% fructose. On the second day, the overnight culture was diluted 100-fold into fresh medium with or without 0.2% glucose and grown at 37 °C until OD<sub>600</sub> reached 0.15-0.25.  $\alpha$ -methylglucoside ( $\alpha$ MG) (Sigma-Aldrich) was then added directly to the culture to the desired concentration. At different time points, fractions of culture were taken out and fixed immediately by mixing with 37% formaldehyde (Fisher Scientific) to a final concentration of 4%.

For *lacZ* mRNA imaging, TK310 cells were grown as described previously in order to compare the copy number of *lacZ* mRNA to previous measurements (31). Cells were grown in M9 minimal medium with thiamine, casamino acids and glucose (M9CAgluc, Teknova). Two *lacZ* mRNA expression levels were chosen: low expression was induced by 1 mM isopropyl  $\beta$ -D-1-thiogalactopyranoside (IPTG, Sigma-Aldrich), and high expression was induced by 1 mM IPTG and 10 mM adenosine 3',5'-cyclic monophosphate (Sigma-Aldrich) (31). Cells were grown at 37 °C and fixed when OD<sub>600</sub> reached 0.2-0.3.

Fixation and permeabilization were performed following the previously published methods (31). Briefly, the cells were mixed with 4% formaldehyde and incubated at room temperature for 30 minutes for fixation, pelleted by centrifugation and then washed twice with 1X PBS by repeated resuspension and centrifugation. Cells were permeabilized with 70% ethanol. 1 mL of 70% ethanol was used for the amount of cells that corresponded to 10mL culture at OD<sub>600</sub> = 0.6. To prevent aggregation, the cell pellet was first resuspended in water, and then 100% ethanol was added to a final concentration of 70%. Cells were incubated at room temperature with rotation for at least 1 hour, and stored at 4 °C before hybridization with oligonucleotide probes.

### 1.3 Single-molecule Fluorescence *in situ* hybridization (smFISH)

Chemically synthesized smFISH probes were designed using Stellaris Probe Designer and ordered from Biosearch Technologies (<http://www.biosearchtech.com>). Probes were 20 nucleotides in length with GC content around 45% and 3' amine modification. 10 nmol of each probe was synthesized and dissolved individually in water to a final concentration of 100  $\mu$ M in 96-well plate.

Equal volumes of each probe were combined for labeling. About 1/9 of the reaction volume of 1M sodium bicarbonate (pH = 8.5) was added such that the final concentration of sodium bicarbonate was 0.1 M. 0.05-0.25 mg of Alexa Fluor 647 or Alexa Fluor 568 succinimidyl ester (Life Technologies) was first dissolved in 1-5  $\mu$ l DMSO and then mixed with the probe solution. The amount of dye was determined such that in the final reaction, the dye was about 20-25 fold in molar excess to probes. The labeling reaction was incubated in the dark at 37 °C with gentle vortexing overnight. Reactions were quenched by adding 1/9 reaction volume of 3M sodium acetate (pH = 5). Labeled probes were purified from unconjugated free dye first by ethanol precipitation and then further purified by P-6 Micro Bio-Spin Column (Bio-Rad). All probes were labeled with more than 80% labeling efficiency.

The hybridization procedure in general followed a previously published protocol (31). 100  $\mu$ l of permeabilized cells in 70% ethanol was used for smFISH hybridization. Cells were washed once with FISH wash solution (10% formamide in 2X SSC) and resuspended in 25  $\mu$ l hybridization buffer (10% dextran sulfate, 1 mg/ml *E.coli* tRNA, 0.2 mg/ml BSA, 2 mM vanadyl ribonucleoside complexes, 10% formamide in 2X SSC). Labeled probes for sRNAs were 50 nM each and for mRNAs were 15 nM each in the final reaction. Hybridization reactions were incubated in the dark at 30 °C overnight. On the second day, the cells were washed three times with FISH wash solution. During each wash, cells were resuspended into 200  $\mu$ l FISH wash solution, and incubated at 30 °C for 30 minutes. After the wash, the cells were pelleted, resuspended into 20  $\mu$ l 4X SSC and stored at 4 °C before imaging. For imaging, cells were immobilized to poly-L-lysine treated 1.0 borosilicate chambered coverglass (Thermo Scientific™ Nunc™ Lab-Tek™). Samples were imaged with imaging buffer (50 mM Tris-HCl, 10% glucose, 1% 2-Mercaptoethanol (Sigma-Aldrich), 20 mg/ml pyranose oxidase (Sigma-Aldrich) (32), and 0.2% catalase (Calbioche) in 2X SSC with pH = 8.0).

#### **1.4 Single-molecule localization-based super-resolution imaging**

3D super-resolution imaging was performed on Olympus IX-71 inverted microscope with a 100X NA 1.4 SaPo oil immersion objective. The 568 nm (Sapphire 568-100 CW CDRH, Coherent) and 647 nm (DL640-100-AL-O, Crystalaser) lasers were used for two-color imaging, and a 405 nm laser (Excelsior 405, Spectra Physics) was used to reactivate both Alexa 647 and Alexa 568 fluorophores. Mechanical shutters (LS6T2, Uniblitz) were used to control each excitation path. All the laser lines were reflected by a dichroic mirror (Di01-R405/488/561/635, Semrock) to the objective. The emission signals were collected by the objective, passed through an emission filter (FF01-594/730-25 from Semrock for Alexa 647 imaging or HQ585/70M 63061 from Chroma for Alexa 568 imaging) and two additional notch filters (NF01-568/647-25X5.0 and NF01-568U-25 from Semrock) to clean up the excitation laser, and imaged on a 512x512 Andor EMCCD camera (DV887ECS-BV, Andor Tech). For 3D imaging, a cylindrical lens with a focal length of 2 m (SCX-50.8-1000.0-UV-SLMF-520-820, CVI Melles Griot) was inserted in the emission path between two relay lenses (100mm and 150mm focal length for each) to induce astigmatism (33). Due to the extra magnification by the relay lenses, each pixel corresponds to 100 nm. The super-resolution imaging setup was equipped with CRIFF (Continuous reflective-interface feedback focus system) (ASI) to eliminate focus drift. Image acquisition was controlled by a custom written data acquisition program (C++).

To image one sample area, a DIC image was first taken. Two-color super-resolution imaging was then performed in a sequential manner with the 647 nm excitation first, followed by the 568 nm excitation. Laser intensity of 647 nm and 568 nm remained constant at  $3,300 \text{ W}\cdot\text{cm}^{-2}$  and  $21,000 \text{ W}\cdot\text{cm}^{-2}$ , respectively. During imaging of each color, the 405 nm laser power was increased gradually in order to compensate for fluorophore photobleaching and maintain signal density such that single molecules were spatially separated. Since high intensity of 405 nm laser partially photobleaches Alexa 568, we used moderate power of 405 nm laser for Alexa 647 reactivation. The highest power of 405 nm laser for reactivating Alexa 647 was  $180 \text{ W}\cdot\text{cm}^{-2}$  and the highest 405 nm laser power for reactivating Alexa 568 was  $600 \text{ W}\cdot\text{cm}^{-2}$ . Imaging was stopped when most of the fluorophores had photobleached at the highest reactivation laser power. Therefore, depending on the actual levels of RNAs in the sample, the number of frames required for imaging until most of the fluorophores photobleached varied. Typically, for SgrS labeled with Alexa 647, frame number varied from  $\sim 1,500$  (with the lowest SgrS copy number) to  $\sim 10,000$  (with the highest SgrS copy number,); for *ptsG* mRNA labeled with Alexa 568, frame number varied from  $\sim 2,000$  to  $\sim 15,000$ .

Fluorescent nanodiamond (140 nm diameter, Academia Sinica, Taipei, Taiwan) (34) was used for mapping of the two channels. The fluorescent nanodiamonds nonspecifically bound to the surface of imaging chambers. They can be excited by both 568 nm and 647 nm lasers and generate localization spots in the final reconstructed images that can be used for mapping of two channels.

## 1.5 Image analysis

The data analysis algorithm was adopted from previous published work from Zhuang's group (33,35), and modified to handle multi-color and 3D images.

### 1. Peak Identification and Fitting

In order to reduce noise from various sources such as the EMCCD sensor or ambient lights, images were first averaged through blurring by Gaussian convolution of 9X9 pixels. To get the average fluctuation of the signal and noise in individual frames, the standard deviation of the intensity in each frame was calculated. All the pixels with intensity values greater than 3.5-4.5 fold of the standard deviation in each frame were identified. Within a 5-by-5 pixel area, local maximum intensity pixels whose intensity values were greater than its 24 surrounding pixels were found to represent the intensity peak of a single fluorophore. To avoid overlapping fluorophores, two additional filters were applied based on the sharpness and roundness of the identified peak. Sharpness is defined as the intensity ratio between the peak and the background. Roundness is defined as the ratio between x variance and y variance in 9X9 pixels. For identified peaks that passed the sharpness and roundness filters, a square region of 19X19 pixels surrounding local maximum intensity pixel was fitted with an Elliptical Gaussian function (33).

$$G(x, y) = h \exp\left(-2 \frac{(x - x_0)^2}{w_x^2} - 2 \frac{(y - y_0)^2}{w_y^2}\right) + b$$

where  $b$  is the background level,  $h$  is the amplitude of the peak,  $w_x$  and  $w_y$  are elliptical widths,  $x_0$  and  $y_0$  are the center coordinates of the peak. Due to the presence of the cylindrical lens for astigmatism,  $w_x$  and  $w_y$  varied from 150 nm to 550 nm after fitting 19X19 square region of pixels with  $G(x,y)$ . If the software failed to fit any 19X19 square region of pixels with a Gaussian function, then that region was discarded. The z-positions of the fluorophores were determined by comparing their  $w_x$  and  $w_y$  values to a calibration curve. The calibration curve was generated from distributions of  $w_x$  and  $w_y$  values from a set of consecutive images of fluorescently labeled single antibodies as objective was moved by defined distance along z direction.

## 2. Drift Correction

Z-drift was prevented in real time by CRIFF. The horizontal drift was corrected during data analysis by fast Fourier transformation (FFT). Super-resolution image was divided into subsets with equal number of frames. FFT was applied on the reconstructed image from each subset. By comparing the center of each transformed image, relative drift among each subset can be determined. By linear interpolation, the drift was corrected through all the frames.

### 1.6 Clustering analysis and copy number calculation

#### 1.6.1 Clustering analysis

A density based clustering analysis algorithm, DBSCAN (15,16), was used to analyze RNA copy numbers. Spots corresponding to individual localization events in a reconstructed super-resolution image were segregated into clusters based on their spatial density. DBSCAN requires two input parameters: Nps and Eps. Spots in the high density core region of the clusters are termed “core points”. The criteria for forming a cluster are that all the core points of a given cluster would be (1) at a distance equal to or less than Eps to each other and (2) surrounded by equal to or more than Nps number of points. Outside the core points are the “border points” that are located at a distance equal to or less than Eps to any of the core points but not to each other. Nps = 2 and Eps = 15 nm were empirically chosen to cluster SgrS (imaged with 9 probes labeled by Alexa 647) images and Nps = 5 and Eps = 25 nm were used to cluster *ptsG* (imaged with 28 probes labeled by Alexa 568) images (Fig. 1C and Movies S1 and S2). After clustering analysis, coordinates of each cluster center and number of spots included in each cluster were recorded for the whole image. Clustered data were then superimposed to the DIC image and the boundaries of individual cells were identified using MATLAB code such that clusters were allocated into individual cells. After clustering analysis and cluster allocation, information derived includes: (1) total number of clusters in each cell, which approximates the total number of RNAs in low copy number cases; (2) number of localization spots in each cluster, which we used to build the characteristic distribution of number of spots per RNA; (3) total number of clustered spots in each cell, which is the product of (1) and (2) and was used for estimating the copy number of RNA per cell; (4) average radius of individual clusters; (5) center coordinates of individual cells.

#### 1.6.2 Baseline correction of the total number of spots per cell

$\Delta sgrS$  (Fig. S14A) and  $\Delta ptsG$  (Fig. S14B) strains were used to estimate the background signal primarily due to probe nonspecific binding for Alexa 647 and Alexa 568 respectively. Samples were prepared, imaged and analyzed the same way as described above. Total numbers of spots per cell for background signal ( $N_0$ ) were calculated from clustering analysis. Due to the stochasticity of fluorophore blinking,  $N_0$  shows a dispersed distribution over the cell population (Fig. S14C). We sorted the cells based on  $N_0$  for each cell and plotted  $N_0$  vs. the percentage of cells ( $x$ ) with number of spots less than  $N_0$  in the data set (i.e. the x-y inversion of cumulative distribution of  $N_0$ ) (Fig. S14D). We empirically described the  $N_0$  vs.  $x$  with double exponential growth:  $N_0 = B + A_1 \cdot \exp((x-x_0)/t_1) + A_2 \cdot \exp((x-x_0)/t_2)$  (Fig. S14D). Depending on the position of a particular cell in the cumulative distribution of total number of spots in each data set ( $x$ ), we used different  $N_0$  for background determined by the fitting curve (Fig. S14D). We subtracted the determined  $N_0$  from the total number of spots in each cell and showed that after correction, distribution of  $N_0$  became a very sharp peak around 0 (Fig. S14E and F). Fig. S14E and F show the probability distribution of total number of spots per cell for the negative controls and examples of low copy number and high copy number samples for  $SgrS$  and  $ptsG$  mRNA, respectively.

### 1.6.3 Copy number calculation

Not all clusters identified from the clustering analysis correspond to single RNA molecules, especially at high copy number case, in which closely neighbored RNA molecules might be clustered into one cluster. In order to calculate the RNA copy number in each cell, we first identified the number of spots for a single RNA molecule ( $N$ ) using samples containing very low copy number RNA ( $\sim 1$  cluster per cell) (Fig. S15A). The assumption is that in the very low copy number RNA case, a single cluster corresponds to a single RNA. Two sources of heterogeneities contribute to the distribution of  $N$ : (1) the heterogeneity in the number of probes bound to each RNA (might not be 100%); and (2) the number of blinking events generated from each labeled probe (Fig. S15A). These two heterogeneities result in the characteristic probability distribution of  $N$  that we used to estimate the RNA copy number per cell (Fig. S15A).

Assuming the spots generated by blinking events from probes hybridized to each RNA molecule are results of a sequence of Bernoulli trials, the probability distribution of  $N$  was fit with negative binomial distribution (Fig. S15B):

$$P(N; r, p) = \binom{N + r - 1}{N} (1 - p)^r p^N \quad (1).$$

After finding  $r$  (number of failures until the trials are stopped) and  $p$  (the probability of success in each trial), we simulated the conditional probability,  $P(N|C)$ , i.e. the probability distribution of having  $N$  spots in the cell with RNA copy number of  $C$ . Assuming distribution of  $N$  generated from multiple RNAs is the convolution of independent and identical negative binomial distribution, we had

$$P(N|C) = P(N; r * C, p) \quad (2).$$

From equation (2), we constructed  $P(N|C)$  matrix:

$$P(N|C) = \begin{bmatrix} P(N = 1|C = 1) & \dots & P(N = 1|C = c) \\ \vdots & \ddots & \vdots \\ P(N = n|C = 1) & \dots & P(N = n|C = c) \end{bmatrix} \quad (3).$$

Based on Bayes' theorem, in a cell with total number of spots  $N$ , the probability of having copy number  $C$  is:

$$P(C|N) = \frac{P(N|C)}{\sum_c P(N|C=c)P(C=c)} P(C) \quad (4).$$

Assuming  $P(C)$  is uniform for all possible copy numbers, we had the most likely copy number of  $C$  for cell having  $N$  spots being

$$E(C|N) = \frac{\sum_c P(N|C=c)c}{\sum_c P(N|C=c)} \quad (5)$$

We also used the average number of spots per RNA from fitting with negative binomial distribution to calculate the copy number, similar to the usage of intensity for single RNA as normalization as reported by regular smFISH studies (31). The average RNA copy numbers in various conditions were essentially the same calculated by both means, with variance slightly higher when calculated by using average number of spots per RNA as normalization (data not shown).

We define "correction factor" as the ratio of mean copy number to mean cluster number per cell for each data set. When plotting correction factor as a function of copy number, in the low copy number case, the correction factor was close to 1, suggesting that individual clusters well represented individual RNAs, whereas in the high copy number case, the correction factor deviated more from 1 (Fig. S15C). As a comparison, we also imaged *lacZ* mRNA as in a previous study with regular smFISH (31) (Fig. S15D, Movie S3 and Section 1.2). We obtained copy numbers in both high (~51.3 per cell) and low expression (~1.22 per cell) conditions highly consistent with those of the previous study (31). In addition, at the high expression level, the correction factor was around 10 (Fig. S15C), much higher than for *ptsG* mRNA and SgrS, suggestive of large aggregation of *lacZ* mRNAs possibly corresponding the transcription sites also observed in regular smFISH experiments (31).

We noted that at the very low copy number of SgrS case, the correction factor showed large variation and smaller than 1 (Fig. S15C). This was due to the background correction described above (Section 1.6.2). Single-molecule localization based super-resolution imaging technique is very sensitive to the blinking of any non-specific binding of the probes. We used the knock-out strains for the control of the background signal due to non-specific binding (Fig. S14) and subtracted the false positive spots from the total number of spots per cell. Since we used lower threshold for clustering analysis of SgrS due to fewer probes used, a relatively larger fraction of total number of spots per cell was attributed to the background signal and subtracted, resulting a final estimation of RNA copy number per cell smaller than the identified number of cluster per cell and therefore a smaller than 1 correction factor on average. This indicates that the accuracy

in copy number determination will be lower for the low copy number case, especially when smaller number of probes are used (such as in SgrS).

### 1.7 Quantitative PCR

Cells were grown as described for the time-course experiments. At each time point, 1 ml of culture was added directly to 120  $\mu$ l of 37% formaldehyde for fixation, and then later used to measure OD<sub>600</sub> for each time point for the calculation of cell number. Another 1 ml of culture was taken, kept on ice and spun down at 4 °C at 7,000 Xg for 1 min. The cell pellet was then resuspended in 100  $\mu$ l of 1 mg/ml lysozyme in TE buffer (10 mM Tris-HCl and 1mM EDTA), mixed by vortexing at room temperature for 10 seconds, and incubated at room temperature for 5 minutes with gentle vortexing. Total RNA was extracted from the lysozyme treated cells using RNeasy mini kit (Qiagen) according to the manufacturer's protocol. 1 ml culture of OD<sub>600</sub> around 0.2 to 0.3 usually gave around 15-30  $\mu$ g of total RNA. Any genomic DNA contamination in the total RNA was removed with TURBO DNase (Ambion). 50 ng of DNase-treated total RNA was then used to generate cDNA with iScript™ cDNA Synthesis Kit (Bio-Rad). Around 1%-10% of the generated cDNA was used for qPCR with primer sets corresponding to *ptsG* mRNA, SgrS as well as 16S rRNA for each sample (Table S3).

A standard curve for absolute quantification was generated using an *in vitro* transcribed RNA, specifically the 5' portion of *ptsG* mRNA (first 100 amino acids). mRNA was transcribed from PCR amplified linear DNA template using MEGAscript T7 Kit (Life technologies) and then put through the same procedure as total extracted RNA, including lysozyme treatment, RNA extraction, DNase treatment and cDNA synthesis to control for sample loss during each step of preparation. cDNA of *in vitro* transcribed RNA was diluted by 5-7 orders of magnitude in a 10-fold dilution series to generate a standard curve of copy number vs. quantitation cycle value (Cq). The Cq corresponding to SgrS or *ptsG* mRNA in each sample was compared to the standard curve to convert into copy number per reaction volume. This value was then corrected for the cell number to give copy number per cell (Fig. 1D).

Comparison of the mean copy number of SgrS or *ptsG* mRNA per cell using qPCR and super-resolution imaging showed good agreement (Pearson's R=0.97), with a slightly lower mean for imaging-based quantification (slope = 0.71) (Fig. 1D). One factor that could contribute to the slight discrepancy is that the super-resolution imaging loses signal at the upper- and bottom-most portions of the cell due to the limited z-range (~800 nm in our case).

### 1.8 Colocalization analysis

The results of clustering analysis were subjected to colocalization analysis to estimate the percentage of mRNA colocalized with sRNA. For any mRNA cluster, a 3D spherical volume with radius of R from the center of the cluster was considered. If spots corresponding to sRNA clusters were found in this volume, then this mRNA cluster was considered to be colocalized with sRNA. Since not all clusters corresponded to single mRNAs, the percentage of colocalized mRNA was estimated by the number of spots within the colocalized clusters divided by the number of spots in all mRNA clusters in that cell. The average radius of a *ptsG* mRNA cluster

was ~40 nm from the clustering analysis (data not shown), we therefore used  $R = 40$  nm cutoff for all colocalization analysis.

*ptsG* mRNA labeled with alternating Alexa 647- and Alexa 568-labeled probes (14 of each probe) was imaged as positive control, in which ~70% of the Alexa 568 signal on *ptsG* mRNA has a colocalized Alexa 647 signal (Fig. 2A and B). However, the actual efficiency of colocalization detection may be actually higher than ~70% because the ~30% failure in colocalization detection for the positive control also includes the contribution by the heterogeneity in probe hybridization, i.e. the fraction of mRNA that has only Alexa 568-labeled probes. Nevertheless, this still ensures the reliable colocalization detection in our experiments. Potential error in the rate determination due to incomplete colocalization detection is discussed in Section 2.3.5.

The base-pairing mutant strain was used as negative control (Fig. S1), from which the percentage of colocalization was plotted as a function of SgrS copy number, and fit with linear function ( $y=a*x$ ) as a control for colocalization by chance (Figs. 2A, 2B and S5A). The coefficient,  $a$ , was then used to correct for percentage of colocalization by chance for a given SgrS copy number in all the samples: corrected colocalization = colocalization –  $a * \text{SgrS copy number}$ .

We also calculated and compared the percentage of colocalization in the RNase E mutant strain using  $R=50$  and  $R=60$  nm. Fig. S5B shows the percentage of colocalization in the RNase E mutant strain at different  $R$  cutoffs after correction. Compared to  $R=40$  nm cutoff,  $R=50$  nm and  $R=60$  nm cutoffs gave ~13% and 25% larger percentage of colocalization, respectively, which did not significantly affect our estimation of kinetic parameters.

## 1.9 SgrS and *ptsG* mRNA half-life measurements

Endogenous *ptsG* mRNA degradation was measured using a rifampicin-chase experiment. Wild-type cells were grown overnight in MOPS EZ rich defined medium (TEKnova) supplemented with 0.2% fructose. The next day, the overnight culture was diluted 100-fold into fresh medium with 0.2% glucose and grown at 37 °C until the  $OD_{600}$  reached 0.15-0.25. Rifampicin was added to the culture to a final concentration of 500  $\mu\text{g}/\text{mL}$ . Addition of rifampicin marked the 0 minute time point. Fractions were taken every 2 minutes and fixed immediately as described above (Fig. S3A). SgrS degradation was measured after *sgrS* transcription was stopped by removing  $\alpha\text{MG}$  from the media. The wild-type or the RNase E mutant cells were inoculated and grown as described above to  $OD_{600}$  of 0.15-0.25.  $\alpha\text{MG}$  was added to the culture and the cells were grown for 10 minutes to induce SgrS transcription. Cells were washed twice with cold, fresh medium without  $\alpha\text{MG}$  by repeated centrifugation and resuspension, and resuspended in the same volume of fresh medium pre-incubated at 37 °C, which was considered as the 0 minute time point. Fractions were taken every 2 minutes and fixed right away as described above (Fig. S3B). Samples were imaged and analyzed as described above. Natural log of the copy number was plotted against time and the lifetime of the RNA was estimated from the slope of the linear fitting (Fig. S3C). Degradation rates, determined

by the reciprocal of the lifetimes were reported in Table S4 and discussed in the following section (Section 1.10.1).

## 1.10 Modeling of SgrS-induced *ptsG* mRNA degradation

### 1.10.1 Kinetic model and experimental measurements of certain kinetic parameters

For the wild-type strain, mass-action equations describing the kinetic changes of SgrS, *ptsG* mRNA and SgrS-*ptsG* complex were written as below, including kinetic steps: transcription of SgrS (with rate constant  $\alpha_S$ ) and *ptsG* ( $\alpha_p$ ), endogenous degradation of *ptsG* mRNA ( $\beta_p$ ), degradation of SgrS excluding the co-degradation with *ptsG* mRNA ( $\beta_{S,p}$ ), binding of SgrS to *ptsG* ( $k_{on}$ ), dissociation of SgrS from *ptsG* ( $k_{off}$ ) and RNase E-mediated co-degradation of SgrS-*ptsG* complex ( $k_{cat}$ ).

$$\frac{d[p]}{dt} = \alpha_p - \beta_p[p] - k_{on}[S][p] + k_{off}[Sp] \quad (6),$$

$$\frac{d[S]}{dt} = \alpha_S - \beta_{S,p}[S] - k_{on}[S][p] + k_{off}[Sp] \quad (7),$$

$$\frac{d[Sp]}{dt} = k_{on}[S][p] - k_{off}[Sp] - k_{cat}[Sp] \quad (8),$$

Where  $[p]$ ,  $[S]$  and  $[Sp]$  are the concentrations of *ptsG* mRNA, SgrS and their complex, respectively (Fig. 1E).

Using the super-resolution imaging and analysis platform, we independently measured the endogenous degradation rate of *ptsG* mRNA ( $\beta_p = 0.0041 \pm 0.0008 \text{ s}^{-1}$ ) (Fig. S3 and Section 1.9). Degradation of SgrS was measured by first inducing SgrS production with  $\alpha$ MG for 10 minutes and then removing  $\alpha$ MG from the media (Fig. S3 and Section 1.9). This method specifically stops SgrS synthesis, but allows ongoing synthesis of SgrS target mRNAs, including *ptsG*. We first measured the SgrS degradation rate in the wild-type strain, denoted as  $\beta_{S,total}$  ( $0.0018 \pm 0.0001 \text{ s}^{-1}$ ), which includes both target-dependent and target-independent spontaneous turnover. We then measured the SgrS degradation rate in the RNase E mutant strain (17,18), denoted as  $\beta_{S0}$  ( $0.0014 \pm 0.0003 \text{ s}^{-1}$ ), which includes target-independent spontaneous turnover and other potential RNase E-independent turnover. These degradation rates are all within the range of typical sRNA and mRNA degradation rates (36-40). The difference between  $\beta_{S,total}$  and  $\beta_{S0}$  is close to our experimental variation, suggesting that the loss of SgrS through RNase E-dependent co-degradation with targets accounts for an insignificant fraction of total SgrS turnover. Since co-degradation of SgrS with *ptsG* mRNA is included in  $\beta_{S,total}$  but not in  $\beta_{S0}$ , the degradation rate of SgrS in the absence of co-degradation with *ptsG* mRNA ( $\beta_{S,p}$ ) should fall between  $\beta_{S0}$  and  $\beta_{S,total}$ . We therefore independently set  $\beta_{S0}$  and  $\beta_{S,total}$  as the lower and upper limits of  $\beta_{S,p}$  respectively.

We determined the transcription rate of *ptsG* using  $\alpha_p = \beta_p \times [p]_0$  (Table S4) where  $[p]_0$  is the initial level of *ptsG* mRNA before stress induction in each condition. The reasoning behind this estimation is that in both the base-pairing mutant background (Fig. S1) and the RNase E mutant

background (Fig. S4), with the stress-induced SgrS transcription, *ptsG* mRNA levels remained unchanged, indicating that without SgrS induced-degradation, *ptsG* mRNA reached the equilibrium in the cell. We determined the  $\alpha_p$  in each case independently. Under the same growth condition, the wild-type, base-pairing mutant and the RNase E mutant and  $\Delta hfq$  strains all gave very similar  $\alpha_p$  values (Table S4).

Since co-degradation is blocked in the RNase E mutant strain, we set  $k_{cat} = 0$ :

$$\frac{d[p]}{dt} = \alpha_p - \beta_p[p] - k_{on}[S][p] + k_{off}[Sp] \quad (9),$$

$$\frac{d[S]}{dt} = \alpha_S - \beta_{S0}[S] - k_{on}[S][p] + k_{off}[Sp] \quad (10)$$

$$\frac{d[Sp]}{dt} = k_{on}[S][p] - k_{off}[Sp] \quad (11),$$

We then applied those measured parameters,  $\alpha_p$ ,  $\beta_p$  and  $\beta_{S0}$ , to equations (6-11), and determined the remaining parameters ( $\alpha_S$ ,  $\beta_{S,p}$ ,  $k_{on}$ ,  $k_{off}$  and  $k_{cat}$ ) by fitting the equations to the time courses of both strains (Table S4).

In addition, we also allowed  $k_{cat}$  as a fitting parameter instead of constraining it to be zero in the RNase E mutant strain. Allowing this non-zero  $k_{cat}$  in the RNase E mutant strain had insignificant effect on our estimation on other five parameters (Section 2.1), while including one free parameter improved slightly the overall fitting as expected (Table S5).

### 1.10.2 Parameter search

We used  $R^2$  for parameter search, defined as below:

$$R^2 \equiv 1 - \frac{SS_{res}}{SS_{tot}}$$

Where  $SS_{tot} = \sum_i (y_i - \bar{y})^2$  is the total sum of squares (proportional to the sample variance) and  $SS_{res} = \sum_i (y_i - f_i)^2$  is the residual sum of squares,  $y_i$  is the experimental data and  $f_i$  is the fitted value.

Since sRNA, mRNA and the complex had different mean and variance values, in order not to bias the fitting to a particular molecular species, we used the Poisson weighting ( $SS_{tot}$  and  $SS_{res}$  weighted by  $f_i$ ) in global  $R^2$  calculation. The best set of parameters was determined by the maximizing the global  $R^2$ . Four combinations from two replicates of measurements on the wild-type and the RNase E mutant strains were fit independently and the final parameters were reported as the mean  $\pm$  standard deviation from the four fittings (Table S4). Note that the remaining five parameters were over-determined by six time courses.

Because  $\beta_{S,p}$  was constrained in the parameter search by the experimental measurements (Section 1.10.1), we found that the fitting of SgrS was most sensitive to  $\alpha_S$  (Fig. S16A) and was

relatively insensitive to  $k_{on}$ ,  $k_{off}$  and  $k_{cat}$  (Fig. S16B and C); whereas modeling of *ptsG* mRNA and SgrS-*ptsG* complex was sensitive to all parameters (Fig. S16).

We checked the parameter set ( $\alpha_S$ ,  $\beta_{S,p}$ ,  $k_{on}$ ,  $k_{off}$  and  $k_{cat}$ ) determined by optimization of global  $R^2$  by calculating the  $R^2$  for kinetic curves of individual species (Table S5). We noted that for SgrS-*ptsG* complex in the wild-type strain,  $R^2$  was not a good estimator for the goodness of fitting because the level of complex in the wild-type strain was close to the background, the total variance became too small. In such cases, we calculated  $\chi^2$  as

$$\chi^2 \equiv \sum_i \frac{(y_i - f_i)^2}{f_i}$$

and reported the significance level ( $\alpha$ ) (Table S5).

### 1.11 $K_D$ determination

We determined the apparent dissociation constants ( $K_D$ ) for formations of SgrS-*ptsG* and SgrS-*manXYZ* mRNA complexes in the RNase E mutant strain. Assuming the association and dissociation reached quasi-equilibrium at each time point without co-degradation in the RNase E mutant strain, for *ptsG* mRNA, we had

$$\frac{[Sp]}{[p]} = \frac{k_{on}}{k_{off}} [S] = \frac{1}{K_D} [S]$$

where  $[S]$ ,  $[p]$  and  $[Sp]$  are concentrations of SgrS, *ptsG* mRNA, and SgrS-*ptsG* complex. By fitting  $[Sp]/[p]$  vs.  $[S]$  with linear function (Fig. 3B), we estimated the  $K_D$  of SgrS binding to *ptsG* mRNA to be  $1.0 \pm 0.2 \mu\text{M}$ , consistent with the ratio of  $k_{off}$  to  $k_{on}$  (Table S4). Mean and error were calculated directly from the fitting.

Previous biochemical experiments have identified two binding sites for SgrS on *manXYZ* mRNA and observed efficient degradation only when both binding sites are present (28,41). However our current super resolution imaging and analysis platform cannot yet reliably distinguish the stoichiometry in the complex, therefore the SgrS-*manXYZ* complex we measured in the RNase E mutant strain was the total concentration of complexes containing one or two SgrS molecules. Since

$$\frac{[Sm] + [S_2m]}{[m]} > \frac{[Sm]}{[m]} = \frac{k_{on}}{k_{off}} [S] = \frac{1}{K_D} [S]$$

Where  $[Sm]$  and  $[S_2m]$  are concentrations of SgrS-*manXYZ* complex containing one and two SgrS, respectively, by fitting  $([Sm]+[S_2m])/[m]$  vs.  $[S]$  with linear function (Fig. 3B), the estimated apparent  $K_D$ ,  $2.3 \pm 0.2 \mu\text{M}$ , actually reports the lower limit of  $K_D$  for binding single SgrS to *manXYZ* mRNA.

### 1.12 Localization projection in 2D

Localization analysis was performed through 2D projection along the longitudinal axis onto the cross section of the cell (defined as XY plane) (Fig. S10A). The longitudinal axis passing through the center of the XY plane was defined as the Z axis (Fig. S10A). For projection along the Z axis, 10% of the length of the cell from both ends was cut. ~100-200 cells were overlaid after projection to generate a heat map (Fig. S10B). The radial distance (R) of each spot was calculated in the XY plane and the histogram of R revealed the localization either at the cell periphery or in the cytoplasm (Fig. S10C).

## Supplementary Text

### 2.1 Kinetic model with $k_{\text{off}} = 0$

One key finding suggested by our kinetic model is that the formation of the sRNA-mRNA complex is highly dynamic, characterized by a slow association (with rate constant  $k_{\text{on}}$ ) and a fast dissociation ( $k_{\text{off}}$ ). To test whether including  $k_{\text{off}}$  is necessary in the model in order to explain the experimental data, we first set  $k_{\text{off}} = 0$  while keeping all the other parameters determined for the wild-type and the RNase E mutant strains as in Table S4 (the first two columns) and simulated the kinetic curves for SgrS, *ptsG* mRNA and the complex in both the wild-type and the RNase E mutant strains. The model with  $k_{\text{off}} = 0$  did not fit our experimental data (Fig. S9A). As expected, *ptsG* mRNA was degraded faster when no dissociation of SgrS was allowed in the wild-type strain, while in the RNase E mutant background, the complex accumulated to more than 10-fold higher level than observed experimentally.

We then set  $k_{\text{off}} = 0$  in the fitting, and searched for the rest of the parameters by fitting the six time-course changes of SgrS, *ptsG* mRNA and SgrS-*ptsG* complex in both the wild-type and the RNase E mutant (Fig. S9B). While fitting of SgrS in both wild-type and the RNase E mutant was less sensitive to  $k_{\text{off}}$ , fitting of *ptsG* mRNA in the wild-type strain and SgrS-*ptsG* mRNA complex in the RNase E mutant strain were poor when  $k_{\text{off}} = 0$  (Fig. S9B and Table S5). As illustrated in Fig S16B, reasonable fits of SgrS-*ptsG* complex converge to the diagonal region in the  $R^2$  vs.  $k_{\text{on}}$  and  $k_{\text{off}}$  heat map; i.e.  $k_{\text{off}}$  needs to be ~1000-fold higher than  $k_{\text{on}}$  in order to explain the experimental measurements. Therefore,  $k_{\text{off}} = 0$  had the largest effect on the determination of  $k_{\text{on}}$ . In order to account for the slow accumulation of the complex in the RNase E mutant background,  $k_{\text{on}}$  was determined to be much smaller ( $\sim 6.1 \times 10^3 \text{ (M}^{-1} \cdot \text{s}^{-1})$ ) compared to  $\sim 2.0 \times 10^5 \text{ (M}^{-1} \cdot \text{s}^{-1})$  at non-zero  $k_{\text{off}}$ ). The much smaller  $k_{\text{on}}$  resulted in slower degradation of *ptsG* mRNA in the wild-type strain, again inconsistent with the experimental data.

We estimated the ranges of  $k_{\text{on}}$ ,  $k_{\text{off}}$  and  $k_{\text{cat}}$  that can reasonably model the experiment data with fixed  $\alpha_{\text{S}} = 0.33 \text{ molecule} \cdot \text{s}^{-1}$  and  $\beta_{\text{S,p}} = 0.0014 \text{ s}^{-1}$ . Since modeling of SgrS is not sensitive to the choice of  $k_{\text{on}}$ ,  $k_{\text{off}}$  and  $k_{\text{cat}}$  (Fig. S16A). We defined a “reasonable model” based on global fitting as well as fitting on *ptsG* mRNA and SgrS-*ptsG* complex (Fig. S16B) with the following three criteria: (1) global  $R^2$  was within the top 1% of all parameter sets of  $k_{\text{on}}$ ,  $k_{\text{off}}$  and  $k_{\text{cat}}$ ; (2)  $R^2$  for modeling *ptsG* mRNA (combining data sets of the wild-type and the RNase E mutant strains) was greater than 0.97 (compared to best  $R^2$  of 0.99 for *ptsG* mRNA alone); and (3)  $R^2$  for modeling SgrS-*ptsG* complex was greater than 0.71 (compared to best  $R^2$  of 0.73 for complex alone). These criteria gave  $k_{\text{on}} = (1.2 \sim 4.5) \times 10^5 \text{ (M}^{-1} \cdot \text{s}^{-1})$ ,  $k_{\text{off}} = 0.13 \sim 0.49 \text{ (s}^{-1})$ , and  $k_{\text{cat}} = 0.28 \sim 0.49 \text{ (s}^{-1})$ .

Finally we estimated the potential contribution of non-zero  $k_{\text{cat}}$  in the RNase E mutant strain to the determination of  $k_{\text{on}}$  and  $k_{\text{off}}$ . While the mutant RNase E is deficient in co-degradation of SgrS-*ptsG* complex, it is possible that the complex has endogenous turnover or other minor degradation pathways. To test this possibility, we made  $k_{\text{cat}}$  a fitting parameter instead of constraining it to be zero in the RNase E mutant strain in the parameter search (Section 1.10). The co-degradation rate of SgrS-*ptsG* complex in the RNase E mutant strain was estimated to

be  $\sim 0.0067 \text{ s}^{-1}$ , much slower compared to RNase E-mediated co-degradation rate ( $\sim 0.4 \text{ s}^{-1}$ ) in the wild-type strain. Allowing this much slower  $k_{\text{cat}}$  in the RNase E mutant strain did not affect our determination of  $k_{\text{on}}$  ( $\sim 1.9 \times 10^5 \text{ (M}^{-1}\cdot\text{s}^{-1})$ ) compared to  $\sim 2.0 \times 10^5 \text{ (M}^{-1}\cdot\text{s}^{-1})$  when  $k_{\text{cat}} = 0$  in the RNase E mutant strain) and  $k_{\text{off}}$  ( $\sim 0.16 \text{ s}^{-1}$  compared to  $\sim 0.20 \text{ s}^{-1}$  when  $k_{\text{cat}} = 0$  in the RNase E mutant strain) (Tables S4 and S5).

## 2.2 Validation of the kinetic model and the effect of Hfq deletion

We tested the kinetic model under several other conditions. We first lowered the concentration of  $\alpha\text{MG}$  to 0.25% (Fig. S6), and searched for the transcription rate of SgrS ( $\alpha_{\text{S}}$ ) while all the other parameters were kept the same.  $\alpha_{\text{S}}$  was dropped to  $0.18 \pm 0.02 \text{ molecule}\cdot\text{s}^{-1}$ , and the slower transcription of SgrS dictated the slower induced degradation of *ptsG* mRNA by SgrS (Table S4, Figs. S6 and S8). We next left out glucose from the growth media (Fig. S7). In this scenario, we observed a  $\sim 3$ -fold decrease in the steady-state level of *ptsG* mRNA before induction of SgrS, consistent with the reports that the presence of glucose increases *ptsG* transcription (42,43). Since glucose is not known to affect endogenous turnover of *ptsG* mRNA in a wild-type strain, we estimated  $\alpha_{\text{p}}$  in the absence of glucose to be  $0.04 \pm 0.01 \text{ molecule}\cdot\text{s}^{-1}$  by  $\alpha_{\text{p}} = \beta_{\text{p}} \times [\rho]_0$ . In addition to reducing *ptsG* transcription, the absence of glucose enhanced induction of SgrS by  $\alpha\text{MG}$  (Table S4, Figs. S7 and S8). Since glucose and  $\alpha\text{MG}$  compete for the same transporter, in the absence of glucose  $\alpha\text{MG}$  is taken up more rapidly (44,45). In this case,  $\alpha_{\text{S}}$  increased to  $0.495 \pm 0.007 \text{ molecule}\cdot\text{s}^{-1}$ , and the predicted time-dependent change of SgrS and *ptsG* mRNA agreed well with the experimental data without tuning additional parameters except for  $\alpha_{\text{S}}$  and  $\alpha_{\text{p}}$ . These experiments validated our estimation of  $k_{\text{on}}$ ,  $k_{\text{off}}$  and  $k_{\text{cat}}$ .

Hfq protein functions in sRNA-based regulation by stabilizing the sRNA or promoting its annealing with the target mRNA (20,46). We therefore fit the time-course measurements of SgrS and *ptsG* mRNA in the  $\Delta\text{hfq}$  background, considering the possibility of enhanced SgrS degradation rate and the probable reduced SgrS-*ptsG* mRNA association rate and searching for  $\beta_{\text{S,p}}$  and  $k_{\text{on}}$ , while keeping the rest of parameters the same as for the wild-type case. Our results (consistent with previously published results (10,47) revealed that for SgrS, Hfq has a major effect on stability. In the absence of Hfq, the degradation rate of SgrS was increased by about 20-fold (Table S4, Figs. S2 and S8). The fitting also suggested a slight decrease in the SgrS-*ptsG* mRNA association rate in the absence of Hfq (Table S4). However, the estimation of  $k_{\text{on}}$  might be less accurate than for  $\beta_{\text{S,p}}$  given that the fitting quality was much less sensitive to the change of  $k_{\text{on}}$  in the  $\Delta\text{hfq}$  background.

## 2.3 Potential errors in the parameter determination

### 2.3.1 Translation of *sgrS* RNA to produce SgrT

We reported a generic model that can explain the observed kinetic behavior without the requirement for additional intermediates or other configurations, and all the kinetic rates can be validated by the experimental data. It is worth mentioning that as a dual-function sRNA, *sgrS* RNA is also translated to produce a short peptide SgrT (48); however, this additional configuration of SgrS does not conflict with our current model. In our imaging experiments and the modeling, we counted all SgrS present in the cell at given time regardless of translational

status, as our method cannot distinguish sRNAs associated with the ribosome from those that are not. Even though the fraction of SgrS being translated will reduce the effective concentration of SgrS for regulation, this is taken into account by the  $k_{on}$  in our model, which represents the apparent rate constant for target search that essentially includes all kinetic steps potentially involved, such as any dynamic equilibrium between free (used for regulation) and the translated forms, diffusion and annealing to the target, *etc.* Therefore, at the systems level, for a given concentration of SgrS, the apparent association rate with the *ptsG* mRNA is still  $k_{on} \cdot [SgrS]$  ( $s^{-1}$ ). In addition, it has been shown that SgrS is not detectably translated under our reported growth conditions (14); thus, we expect the any contribution from translation is insignificant.

### 2.3.2 *ptsG* mRNA degradation induced by the basal level of SgrS under the uninduced condition

We measured endogenous degradation of *ptsG* mRNA by inhibiting transcription under the uninduced condition (no  $\alpha$ MG, and therefore only basal level of SgrS). In this case, the average copy number of SgrS was measured to be  $\sim 2.5$  per cell (at time of 0 min in the kinetic measurements). We estimated the contribution of *ptsG* mRNA degradation by co-degradation with the basal level of SgrS by

$$\frac{k_{cat}k_{on}[SgrS]_{uninduced}}{k_{off} + k_{cat}}$$

to be  $\sim 0.00033 s^{-1}$ , which is negligible compared to the measured endogenous turnover rate of *ptsG* mRNA ( $0.0041 \pm 0.0008 s^{-1}$ )

### 2.3.3 Influence of SgrS-*ptsG* complex on the measurement of $\beta_{S0}$

When co-degradation is blocked in the RNase E mutant background, a fraction of SgrS exists in the complex form. However, the fraction is estimated to be very small and should not significantly affect our determination of  $\beta_{S0}$ . The reasons are as following: (1) SgrS-mRNA complexes are unstable as suggested in our model for both SgrS-*ptsG* and SgrS-*manXYZ*. SgrS rapidly dissociates from the complex back into the free form that follows the degradation rate of  $\beta_{S0}$ . (2) In the RNase E mutant, the average copy number of the SgrS-*ptsG* complex is  $\sim 3$  per cell at later time points, constituting only about 2% of the SgrS level ( $\sim 150$  per cell at the same time points). And the copy number of SgrS-*manXYZ* complex is even smaller (Fig. 3B). In addition, the difference between  $\beta_{S, total}$  and  $\beta_{S0}$  is close to our experimental variation, suggesting that the loss of SgrS through RNase E-dependent co-degradation with targets and the contribution from the degradation of SgrS in the complex form account for an insignificant fraction of total SgrS turnover.

### 2.3.4 Efficiency of RNA detection

The efficiency of RNA detection by super-resolution imaging was estimated by comparing to qPCR. On average, imaging quantification gave  $\sim 70\%$  of the qPCR quantification. One factor that could contribute to the slight discrepancy is that the super-resolution imaging loses signal at the upper- and bottom-most portions of the cell due to the limited z-range ( $\sim 800$  nm in our case). However, qPCR measurements will also be subject to systematic error due to

various steps during the sample preparation. Based on the 16S rRNA measured in qPCR (~100,000 copies per cell) and the reported value in the literature for *E.coli* at exponential phase in rich media (~70,000 (49)), the RNA copy number measured by qPCR might be slightly over-estimated. Overall, the comparison between the two methods suggests that the RNA detection efficiency by imaging is greater than 70%. We used 70% to correct the copy numbers of both SgrS and *ptsG* mRNA and estimated the kinetic parameters described in Section 1.10. Among the parameters,  $\beta_{S,p}$ ,  $k_{off}$  and  $k_{cat}$  remained unchanged.  $\alpha_S$  was the most affected ( $0.47 \pm 0.01$  molecule $\cdot$ s $^{-1}$ , compared to  $0.33 \pm 0.01$  molecule $\cdot$ s $^{-1}$  without correction), and  $k_{on}$  was slightly affected ( $(1.4 \pm 0.1) \times 10^5$  (M $^{-1}\cdot$ s $^{-1}$ ), compared to  $(2.0 \pm 0.2) \times 10^5$  (M $^{-1}\cdot$ s $^{-1}$ ) without correction).

### 2.3.5 Efficiency of colocalization detection

We also examined the effect of colocalization detection efficiency on determination of the kinetic rates. We corrected the colocalization by 70% (Fig. 2) and estimated the parameters as described in Section 1.10. While  $\alpha_S$ ,  $\beta_{S,p}$ , and  $k_{on}$  remained unchanged, higher colocalization, corresponding to a higher cellular level of the SgrS-*ptsG* complex, had the largest effect on the estimation of  $k_{off}$  ( $0.13 \pm 0.03$  s $^{-1}$ , compared to  $0.20 \pm 0.04$  s $^{-1}$  without correction), and a smaller effect on the estimation of  $k_{cat}$  ( $0.3 \pm 0.1$  s $^{-1}$ , compared to  $0.4 \pm 0.1$  s $^{-1}$  without correction). The largest error contributed by the efficiency of colocalization detection is about 35% in  $k_{off}$ , close to our experimental variation.

## 2.4 Kinetic properties of SgrS-induced *manXYZ* mRNA degradation

Previous biochemical experiments have identified two binding sites for SgrS on *manXYZ* mRNA and observed efficient degradation only when both binding sites are present (28,41). However due to the sensitivity of the biochemical assay used, the possibility that binding of SgrS at individual sites might inefficiently trigger degradation cannot be excluded. To describe the kinetics of SgrS-induced *manXYZ* mRNA degradation, the simplest model is as below, in which co-degradation is only allowed when both SgrS RNAs bind to *manXYZ*.

$$\frac{d[m]}{dt} = \alpha_m - \beta_m[m] - k_{on_1}[S][m] + k_{off_1}[Sm] \quad (12),$$

$$\frac{d[S]}{dt} = \alpha_S - \beta_{S,m}[S] - k_{on_1}[S][m] - k_{on_2}[S][Sm] + k_{off_1}[Sm] + k_{off_2}[S_2m] \quad (13),$$

$$\frac{d[Sm]}{dt} = k_{on_1}[S][m] - k_{off_1}[Sm] - k_{on_2}[S][Sm] + k_{off_2}[S_2m] \quad (14),$$

$$\frac{d[S_2m]}{dt} = k_{on_2}[S][Sm] - k_{off_2}[S_2m] - k_{cat}[S_2m] \quad (15),$$

where  $[m]$ ,  $[S]$ ,  $[Sm]$  and  $[S_2m]$  are the concentrations of *manXYZ* mRNA, SgrS, their complex containing one SgrS and two SgrS molecules, respectively.  $\alpha_S$  and  $\alpha_m$  are the rate constants for SgrS and *manXYZ* transcription.  $\beta_m$  and  $\beta_{S,m}$  are the endogenous degradation of *manXYZ* mRNA and SgrS excluding the co-degradation with *manXYZ* mRNA.  $k_{on_1}$ ,  $k_{off_1}$ ,  $k_{on_2}$  and  $k_{off_2}$  are rate constants for the first and second SgrS binding to and dissociation from *manXYZ* mRNA, and  $k_{cat}$  is the rate constant for the co-degradation of the complex.

This simplest kinetic scheme adds two additional parameters into the modeling; however, our current super resolution imaging and analysis platform cannot yet reliably distinguish the

stoichiometry in the complex, and therefore cannot measure  $[Sm]$  and  $[S_2m]$ . Given that the number of observables is less than the free parameters in model, we cannot determine the full parameter set. However, the ability to measure the complex formation regardless of the stoichiometry still enabled us to estimate the lower limit of the apparent  $K_D$  (Section 1.11). We observed a slower rate of complex formation and a larger apparent  $K_D$  for SgrS binding to *manXYZ* mRNA, consistent with the slower SgrS-induced mRNA degradation. We therefore propose that target search kinetics contributes to the setting of the regulatory priority among different target mRNAs by the same sRNA species.

We then attempted to estimate the kinetic rates using the approximation with single-binding regulation used for *ptsG* mRNA (Section 1.10). We considered the *manXYZ* degradation in the wild-type strain in the absence of glucose (since *manXYZ* did not show significant induced degradation by SgrS in the presence of glucose) and together with RNase E mutant strain and determined the parameter set ( $\alpha_S$ ,  $\beta_{S,m}$ ,  $k_{on}$ ,  $k_{off}$  and  $k_{cat}$ ) as described for *ptsG* mRNA (Fig. S17):  $\alpha_S = 0.34 \pm 0.02$  (molecule $\cdot$ s $^{-1}$ ),  $\beta_{S,m} = 0.0014$  (s $^{-1}$ ),  $k_{on} = (1.7 \pm 0.7) \times 10^5$  (M $^{-1}$  $\cdot$ s $^{-1}$ ),  $k_{off} = 0.4 \pm 0.1$  (s $^{-1}$ ),  $k_{cat} = 0.06 \pm 0.02$  (s $^{-1}$ ). Note that  $k_{cat}$  is the apparent rate constant for catalytic step that actually includes the second binding and the co-degradation.

The dissociation constant  $K_D$  was calculated to be 2.4  $\mu$ M using  $k_{on}$  and  $k_{off}$  from the modeling, which is consistent with the lower limit of  $K_D$  extracted in Fig. 3B (Section 1.11). While the locations of the base-pairing region and the Hfq binding site on the mRNA will affect the target search kinetics, the fact that *manXYZ* mRNA contains less complementary bases to SgrS in both base-pairing regions compared to *ptsG* mRNA also partially explains the larger  $K_D$  (primarily originated from larger  $k_{off}$ ) observed for *manXYZ* mRNA (28,41). It remains to be investigated how the differences in the target search kinetics are linked to the sequence and structural features of different target mRNAs.

It is interesting to note that the apparent  $k_{cat}$  that includes the second target site search and the catalytic step is still 4-5 fold faster than the first binding at 100 copies of SgrS (0.017 s $^{-1}$ ), which indicates that the first binding event may increase the probability of the second binding event by an unknown mechanism. However, again, the limit of our imaging sensitivity cannot provide concrete evidence for this potential cooperative binding mechanism. To summarize, determinants for hierarchical regulation of targets are impacted by the molecular mechanism of regulation of each target. Nevertheless, our data indicate that target search kinetics at least partially contributes to the hierarchical regulation. In the case of *manXYZ* mRNA, the larger apparent  $K_D$  and the requirement for two SgrS binding events together set its lower priority in the regulatory network of SgrS.

## 2.5 Justification of using mean copy number in the modeling

We used the mean values of SgrS, *ptsG* mRNA and SgrS-*ptsG* complex to determine the kinetic rates in the generic kinetic model in a deterministic way. However, one concern is that, as computationally predicted for enzyme-catalyzed bimolecular reactions in the cell, when the association of two components, with balanced production rates, is subjected to irreversible degradation, the variations in the two components are strongly coupled, and at the single-cell

level, the levels of the two components demonstrate anti-correlation (50). If this was also the case for SgrS-induced *ptsG* mRNA degradation, then  $k_{on}\langle\text{SgrS}\rangle\langle\text{ptsG}\rangle$  (where  $\langle\text{SgrS}\rangle$  and  $\langle\text{ptsG}\rangle$  are the mean copy numbers over cell population) cannot correctly represent the mean value of  $\langle\text{SgrS-ptsG}\rangle$  (mean copy number of the complex over the cell population), resulting in inaccurate estimation of the rate constants for target search.

We therefore plotted the *ptsG* mRNA vs. SgrS levels in individual cells for the data at 4 minute and 6 minute, when significant degradation of the mRNA was observed for the wild-type strains (Fig. S18), and there was no clear anti-correlation at the individual cell level. We suspect that the lack of anti-correlation between SgrS and *ptsG* mRNA may be due to the following reasons: (1) SgrS has more than one target mRNA, and therefore the coupling between the two will be less tight compared to enzymatic reactions where only interactions between two components are considered (i.e. no other target is involved) (50). (2) The transcription (production) rates of SgrS and *ptsG* mRNA were not the same in most of our experimental cases, while highly anti-correlated behavior was predicted under the conditions where the production rates of both components were the same (50). More importantly, the transcription burstiness in both SgrS and *ptsG* mRNA may cause additional uncoupling between sRNA and mRNA in individual cells.

Because we did not observe clear anti-correlation between sRNA and mRNA at the single cell level, we think it is still fair to use the mean copy number for estimating the kinetic parameters over the cell population. However, a stochastic model considering the transcription burstiness, the localization effect and any other source of fluctuation will further refine the kinetic model and will reveal additional properties in terms of any stochasticity in the regulatory process.

## 2.6 RNase E mutant strain

We used an RNase E mutant carrying the C-terminal truncation to block the co-degradation step in the kinetic model. This mutant lacks the last 360 amino acids, the entire C-terminal scaffold domain and therefore loses its ability to interact with Hfq and several components of the degradosome (17,18,51). The *rne701* mutant has been well characterized by the Aiba laboratory. This group discovered that endogenous *ptsG* degradation is unaffected while SgrS-induced *ptsG* degradation is abrogated in this mutant background (17,18,51). Our experiments with this mutant confirmed previous observations in both LB medium and MOPS EZ rich defined medium supplemented with 0.2% fructose and 0.2% glucose (referred as +glucose medium). The latter growth condition was used to build the kinetic model in this study. Surprisingly, we observed that in MOPS EZ rich defined medium supplemented with 0.2% fructose only (referred as -glucose medium), cellular levels of *ptsG* mRNA in this RNase E mutant background were much higher than the wild-type case in the same growth medium, and after SgrS induction, the cellular level of *ptsG* mRNA dropped over time. In contrast, in this same RNase E mutant background we still observed the abrogation of the SgrS-induced degradation of *manXYZ* mRNA in the -glucose medium (data not shown). The reason for this phenotype is entirely unclear. We postulate that given that RNase E is one the “master” RNA processing enzymes in *E. coli* and interacts with many proteins involved in various cellular pathways (for example, enolase in glycolysis (17,52)), the effect of mutations in RNase E on mRNA endogenous

turnover as well as sRNA-induced degradation may be in general mRNA dependent and growth medium dependent. For building the kinetic model in the current work, we performed all experiments in the +glucose medium, and used these data as training sets. The  $k_{on}$ ,  $k_{off}$  and  $k_{cat}$  we obtained from +glucose medium of SgrS-*ptsG* pair can directly predict SgrS-induced *ptsG* degradation kinetics in the wild-type strain in -glucose medium.

## Supplementary Tables

**Table S1. Bacterial strains used in this work**

<b>Name</b>	<b>Description</b>	<b>Source/reference</b>
<b>DJ480</b>	MG1655 $\Delta/lac$ X74, used as wild-type strain in this study.	D. Jin, National Cancer Institute
<b>CV104</b>	$\Delta sgrS$	(10)
<b>CS196</b>	$\Delta ptsG$	This study (Materials and Methods)
<b>CS123</b>	DJ480 strain carrying G178C/G176C mutations on <i>sgrS</i>	(13,14)
<b>DB138</b>	JH111 strain with $\Delta hfq$	(47)
<b>TM528</b>	rne701-FLAG-cat, RNase E mutation with C-terminal truncation	(17)
<b>TK310</b>	$\Delta cyaA \Delta cpdA \Delta lacY$ , endogenous <i>lacZ</i> mRNA expressed under $P_{lac}$	(53)

**Table S2. Sequences of smFISH probes <sup>a</sup>**

Target	Sequence (5' to 3')
SgrS	GTGCTGATAAAACTGACGCA ACTTCGCTGTCGCGGTAAAA CTTAACCAACGCAACCAGCA CATGGTTAATCGTTGTGGGA ATCCCACTGCATCAGTCCTT GTCAACTTTCAGAATTGCGG TCAGTCACACATGATGCAGG GCGGGTGATTTTACACCAAT AACCAGCAGGTATAATCTGC
<i>ptsG</i>	GCATCTAAGCGCCCTTTATT GCAGGTTAGCAAATGCATTC ATCAGCGATTTACCGACCTT CTGCCATAACATGCGATACA CATGTTTGCAAAGACGGAAC GACACCGATCGCAAAAATCA GATACGCCATCGTTATTGGT ATGATGCCATAGGCAACAAC AACCACGGCCATGGTTTTAA CAGGTGTTTAGAGGCGATTT TAAACATGTACGCTGCGATC GGCAGCTTAATACGGTAGAA GGCAAAGAAGCCAAGATACT CAGAAATGATCGGCACAAAG CCAAATGAAGGACAGCACAA ACTGAGAGAAGGTCTGGATT CAACGTTTCGATGAAACCGTA GGTGTATTCACCAATCTGCA GGCAGACCGTACATTTTGAA CGGTTTTCTGGTTTAGCAGA AACGATGAAGTCGATCAGAC GCGGAAGATGGTGTAGTAAA CGTTTTTCAGATCCAGTGCTT TCGCTTTTGCATCTTCAGTC TCTTTACCACCAAATGCAGC TACATGCGTCGAGGTTAGTA TTAGTACCGAAAATCGCCTG AGTGGTTACGGATGTACTCA
<i>manXYZ</i> <sup>b</sup>	CCAACCATGTGTGCCTATAA TTTTAAGCAACTGCTCTGCA

	<p> CTGGAACGAAATCGATCCAG  AATCAGCGTTTCGGCATT  CCAAGTGGCGTTGTACTTT  CCTTTAGTGGTGTGCGAGTTT  TGTATCAACGAGAAACAGCA  CTCTTTGTGACGACAATGC  CGCCTGCAATGACTTCATAA  TCCACGAGCATTGGAATGTT  ACCAGTTCATCAAAGCTTGG  TTTCAGTGCTTTCACGCCTT  CGGCTTTTTCAACCGGTTTG  CATTGGTTTTGCCGGAGTTG  TAACCATGTAGTCGTTTGGC  TTGGTTTCTTTGGTCCAGCG  GTGAGCAGTGTCTTACGAAC  TCAACTACGTGTGCTGTTAC  GACGCGAATCATTTTGGCAA  CAGCATATTTCCGGGTTGTTG  AATAACAGCATTACGCGTTC  GCTCTACATCTGTTGGGTTG  AATGCCATACCACCGACGTT  CATCAACCGAAACCGCGTTA  TTGAACGCCTCGATATCTTT  AATACCGCGCGCATTTCAGTT  CATTTTCAGTTTCGGATCGG  CGATTTTGCTGATCAGATCC </p>
<i>lacZ</i>	<p> GTGAATCCGTAATCATGGTC  TATTACGCCAGCTGGCGAAA  AGTATCGGCCTCAGGAAGAT  AATGTGAGCGAGTAACAACC  AGATGAAACGCCGAGTTAAC  ATCTTCCAGATAACTGCCGT  TTAAAGCGAGTGGCAACATG  TTTCGACGTTTCAGACGTAGT  ACCATTTTCAATCCGCACCT  TCTGCTCATCCATGACCTGA  TGGTTCGGATAATGCCAACA  ATCGGTCAGACGATTCATTG  GATCGACAGATTTGATCCAG  TATTCGCAAAGGATCAGCGG  AAACGGGGATACTGACGAAA  TCGGCGTATCGCCAAAATCA  ACGGAAGTGGAAAACTGCT  TTTACCTTGTGGAGCGACAT </p>

	AGCGTCACACTGAGGTTTTTC CGGTAAATTGCCAACGCTT TACGCCAATGTCGTTATCCA GTAATCGCCATTTGACCACT ATAATTCAATTCGCGCGTCC ATTCAGCCATGTGCCTTCTT
--	--

<sup>a</sup> Probes were complementary to sequences across the RNAs.

<sup>b</sup> Since *manXYZ* mRNA is post-processed in the cell to give a smaller *manYZ* mRNA, probes are designed for *manX* region only of the polycistronic mRNA to report the full length of *manXYZ* mRNA (41).

**Table S3. Sequences of qPCR primers**

Target	Sequence (5' to 3')
SgrS	GCTTGAAGGACTGATGCAGTGGGATGACCGC CACCAATACTCAGTCACACATGATGCAGGC
<i>ptsG</i> -1 <sup>a</sup>	GTATCCGTA CTGCCTATCGCAGGTATTCTG CGGATACGCCATCGTTATTGGTAAAGCC
<i>ptsG</i> -2	AGCTGCCGCAATTGCTATCT TACCGGTCAGGAACGAGGTC
<i>ptsG</i> -3	TGGTTGCTGCATTTGGTGGT GCCGGCCTGATCCACTTTAG
16S rRNA	AGGCCTTCGGGTTGTAAAGT ATTCCGATTAACGCTTGAC

<sup>a</sup> Three sets of qPCR primers are used to amplify the 5' region, internal region and 3' region to avoid potential local secondary structure. The average copy number of *ptsG* mRNA per cell is calculated from the average result obtained using these three sets.

**Table S4. Rate constants for SgrS-induced *ptsG* mRNA degradation<sup>a</sup>**

	Wild-type	RNase E mutant	Wild-type	Wild-type	<i>Δhfq</i>
Glucose	+	+	+	-	+
αMG (%)	<b>0.5</b>	<b>0.5</b>	<b>0.25</b>	<b>0.5</b>	<b>0.5</b>
α <sub>S</sub> (molecule·s <sup>-1</sup> )	<b>0.33 ± 0.01</b>	0.33 ± 0.01	0.18 ± 0.02	0.495 ± 0.007	-
β <sub>S</sub> (s <sup>-1</sup> ) <sup>b</sup>	<b>0.0014 ± 0.0003<sup>e</sup></b>	0.0014 ± 0.0003	- <sup>f</sup>	-	0.022 ± 0.009
α <sub>p</sub> (molecule·s <sup>-1</sup> ) <sup>c</sup>	<b>0.12 ± 0.01</b>	0.10 ± 0.01	0.12 ± 0.01	0.04 ± 0.01	0.11 ± 0.01
β <sub>p</sub> (s <sup>-1</sup> )	<b>0.0041 ± 0.0008</b>	0.0041 ± 0.0008	-	-	-
k <sub>on</sub> (M <sup>-1</sup> ·s <sup>-1</sup> ) <sup>d</sup>	<b>(2.0 ± 0.2) × 10<sup>5</sup></b>	(2.0 ± 0.2) × 10 <sup>5</sup>	-	-	(9 ± 4) × 10 <sup>4</sup>
k <sub>off</sub> (s <sup>-1</sup> )	<b>0.20 ± 0.04</b>	0.20 ± 0.04	-	-	-
k <sub>cat</sub> (s <sup>-1</sup> )	<b>0.4 ± 0.1</b>	0	-	-	-

<sup>a</sup> Parameters in the wild-type and the RNase E mutant strains are determined simultaneously by the modeling. Rate constants are reported as mean ± standard deviation from independent fitting on two experimental replicates (Section 1.10).

<sup>b</sup> β<sub>S</sub> refers to β<sub>S,p</sub> in the wild-type and *Δhfq* strains, and β<sub>S0</sub> in the RNase E mutant strain (Section 1.10)

<sup>c</sup> Transcription rate of *ptsG* is estimated using α<sub>p</sub> = β<sub>p</sub> × [p]<sub>0</sub>, where [p]<sub>0</sub> is the initial level of *ptsG* mRNA before stress induction in each condition (Section 1.10).

<sup>d</sup> Copy number per cell is converted to molar concentration for the comparison of k<sub>on</sub> with other studies, with the approximation that one molecule per *E. coli* cell is roughly equal to 1 nM in concentration (36).

<sup>e</sup> 0.0014 s<sup>-1</sup> always gives the best fit in the modeling. The standard deviation is reported directly from the measured rate constant for SgrS degradation in the RNase E mutant strain (Sections 1.9 and 1.10).

<sup>f</sup> Parameters marked by “-“ refer to the same value as in the case of wild-type strain in the presence of glucose with induction of SgrS by 0.5% αMG (in bold italic).

Table S5.  $R^2$  and  $\chi^2$  of modeling <sup>a</sup>

	Target mRNA	Glu	$\alpha$ MG (%)	Global $R^2$	$R^2$ for SgrS	$R^2$ for mRNA	$R^2$ for S-m	$\chi^2$ for S-m	$\alpha$ for S-m
WT	<i>ptsG</i>	+	0.5	0.975	0.998	0.991	-	1.36	0.025
RNase E mutant	<i>ptsG</i>	+	0.5	0.975	0.998	0.838	0.778	-	-
WT	<i>ptsG</i>	+	0.25	0.987	0.994	0.934	-	1.67	0.001
WT	<i>ptsG</i>	-	0.5	0.999	0.999	0.946	-	1.15	0.001
$\Delta hfq$	<i>ptsG</i>	+	0.5	0.872	0.916	0.848	-	3.19	0.025
WT with $k_{off} = 0$	<i>ptsG</i>	+	0.5	0.994	0.998	0.786	-	2.30	0.1
RNase E mutant with $k_{off} = 0$	<i>ptsG</i>	+	0.5	0.994	0.996	0.905	0.687	-	-
WT with $k_{cat} \neq 0$ in RNase E mutant	<i>ptsG</i>	+	0.5	0.997	0.998	0.991	-	1.13	0.025
RNase E mutant with $k_{cat} \neq 0$	<i>ptsG</i>	+	0.5	0.997	0.998	0.984	0.746	-	-
WT	<i>manXYZ</i>	-	0.5	0.999	0.999	0.959	-	0.42	0.001
RNase E mutant	<i>manXYZ</i>	+	0.5	0.999	0.994	0.899	0.700	-	-

<sup>a</sup> Global  $R^2$  is optimized in parameter search, and the determined parameter set is used to calculate  $R^2$  and  $\chi^2$  for modeling of individual kinetic curve (Section 1.10).

Supplementary Figures

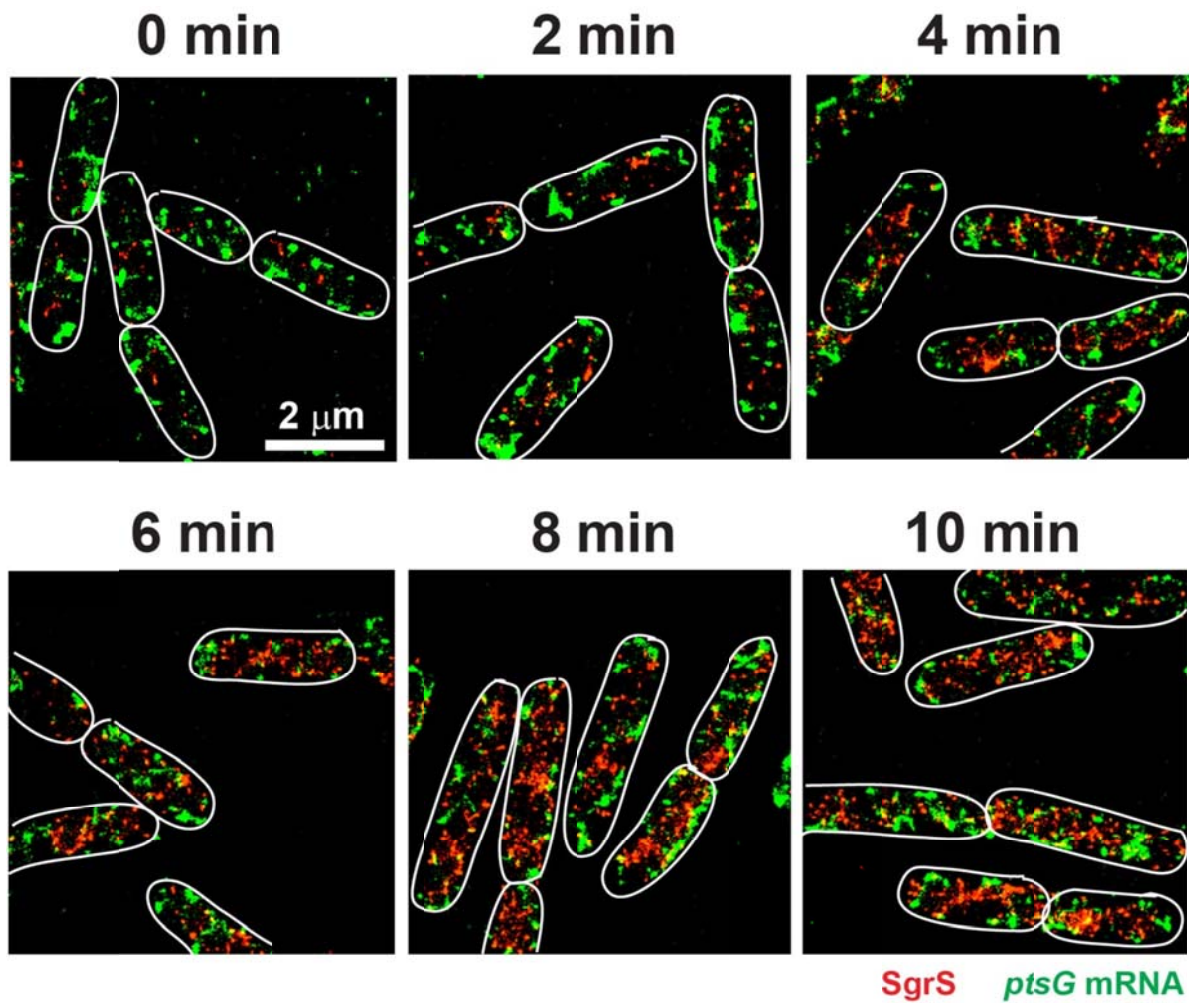
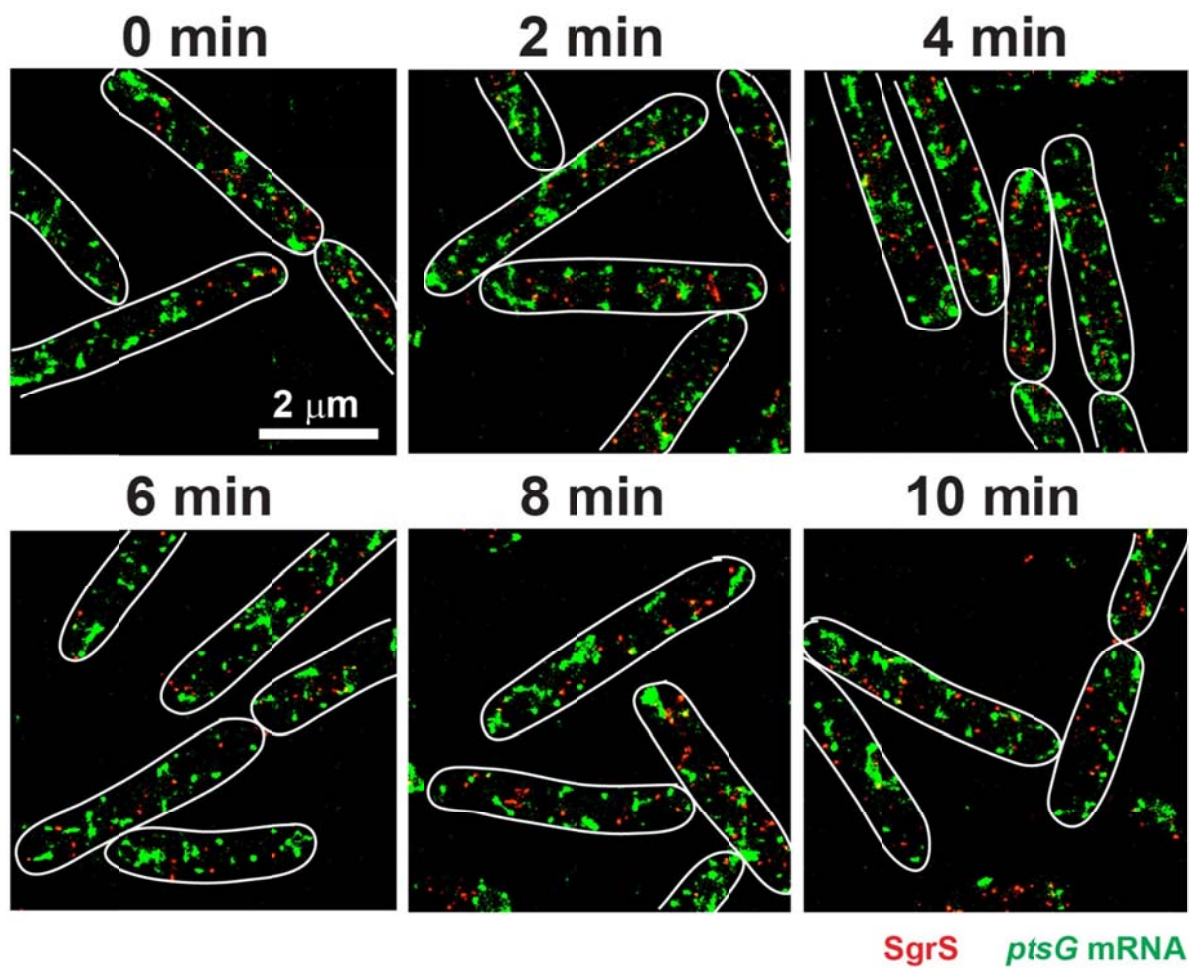
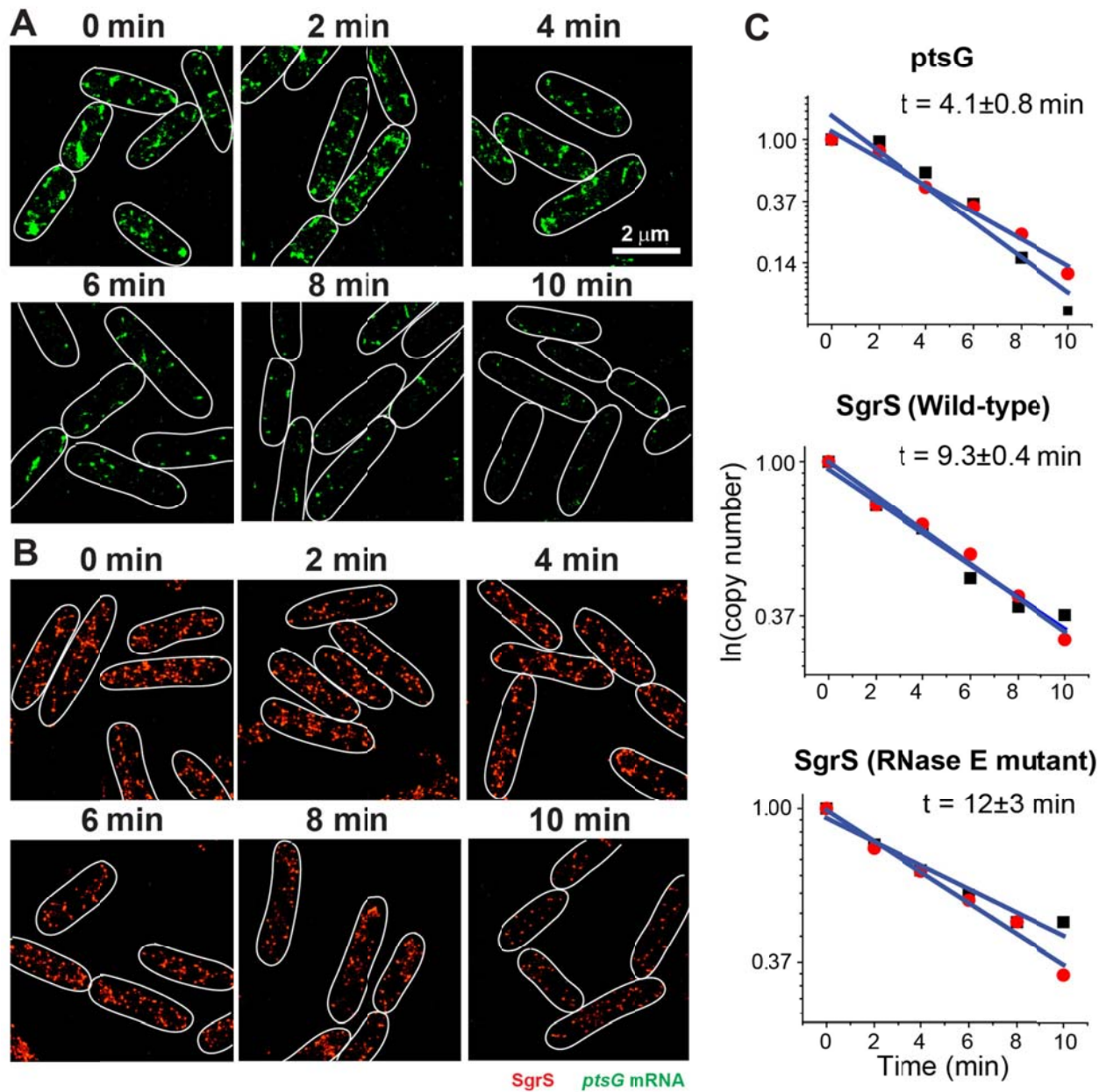


Figure S1. Time-dependent changes of SgrS (red) and *ptsG* mRNA (green) in the base-pairing mutant strain. Description of the figure is the same as in Fig. 1A.



**Figure S2. Time-dependent changes of SgrS (red) and *ptsG* mRNA (green) in the  $\Delta hfq$  strain.** Description of the figure is the same as in Fig. 1A.



**Figure S3. Measurements of the RNA lifetime.** (A) *ptsG* mRNA degradation in the wild-type strain. (B) SgrS degradation in the wild-type strain. (C) Calculation of the RNA lifetime. Black squares and red dots represent two independent measurements (mean value from ~150 cells in each measurement). Copy numbers are normalized to time 0 in each case. See Section 1.9 for detailed information.

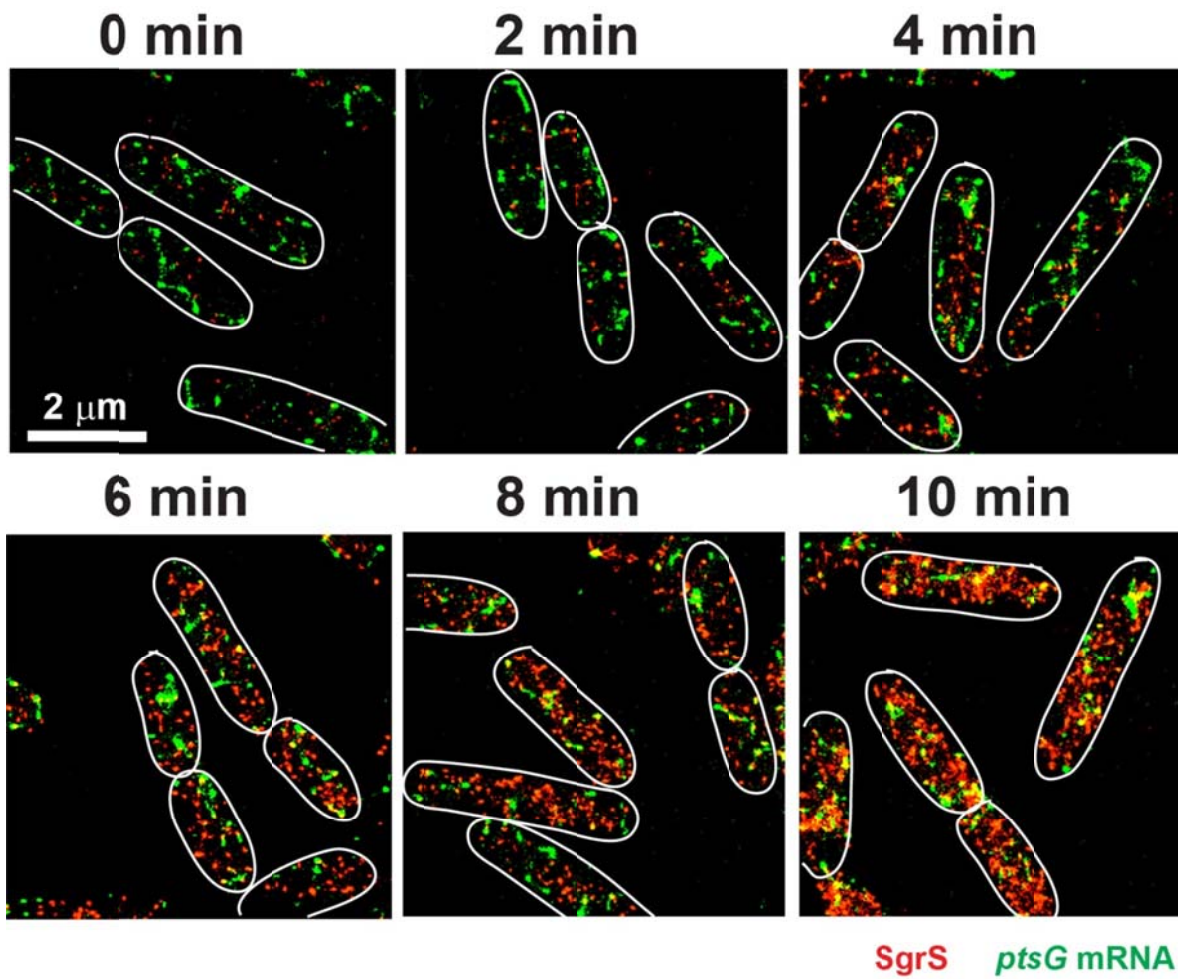


**Figure S4. Time-dependent changes of SgrS (red) and *ptsG* mRNA (green) in the RNase E mutant strain.** Description of the figure is the same as in Fig. 1A.

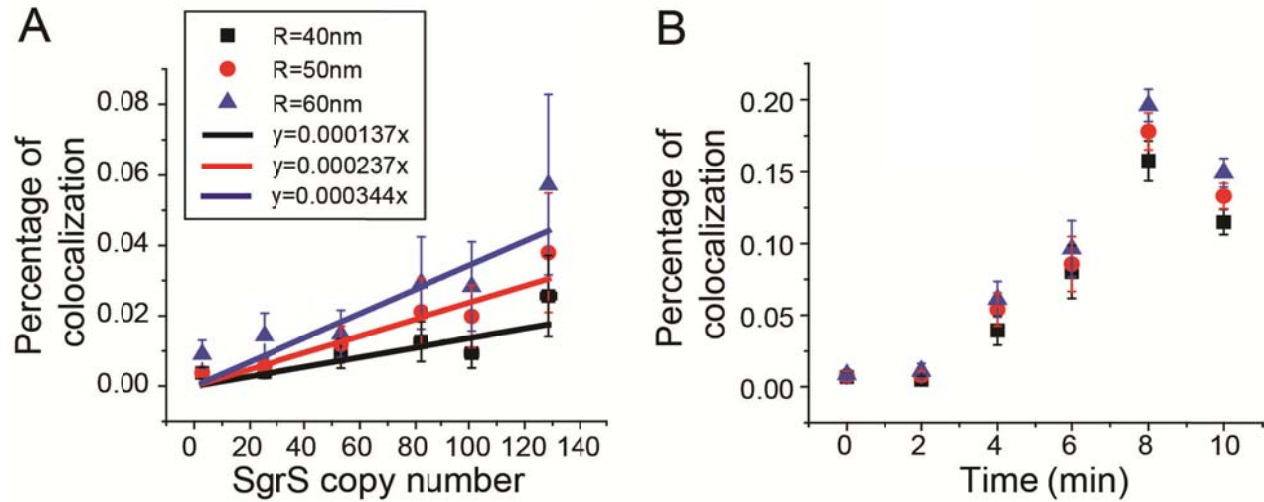


**Figure S5. Colocalization analysis with different R cutoffs.** (A) Percentage of colocalization in base-pairing mutant strain with different R cutoffs as a function of mean SgrS copy number. Each plot is fit with linear function for correction of colocalization by chance. (B) Comparison of percentage of *ptsG* mRNA colocalized with SgrS in the RNase E mutant strain with three different R cutoffs. Percentages are all corrected with corresponding baselines in (A). Error bars are standard deviations from 4-8 images.

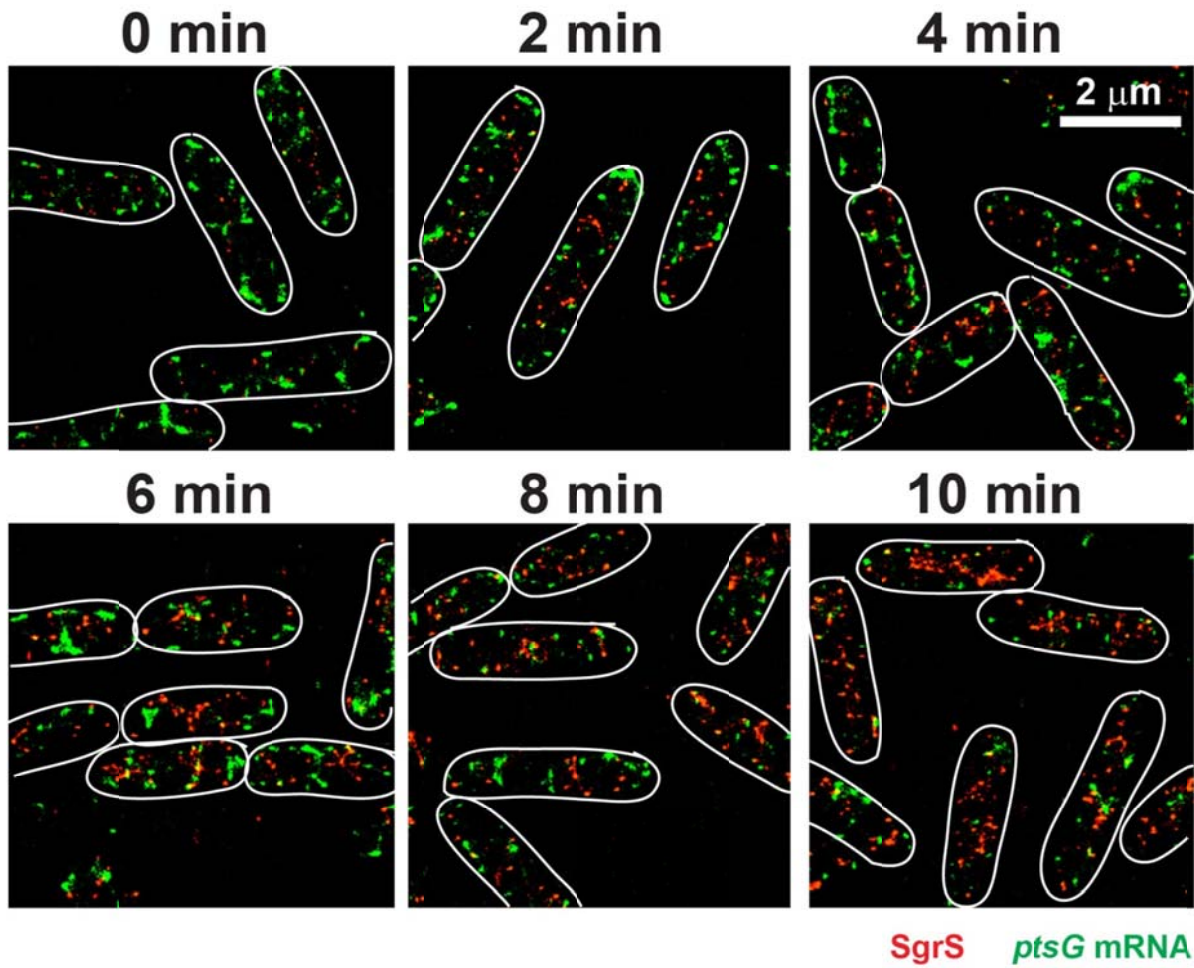


**Figure S6.** Time-dependent changes of SgrS (red) and *ptsG* mRNA (green) in the wild-type strain induced by 0.25%  $\alpha$ MG. Description of the figure is the same as in Fig. 1A.

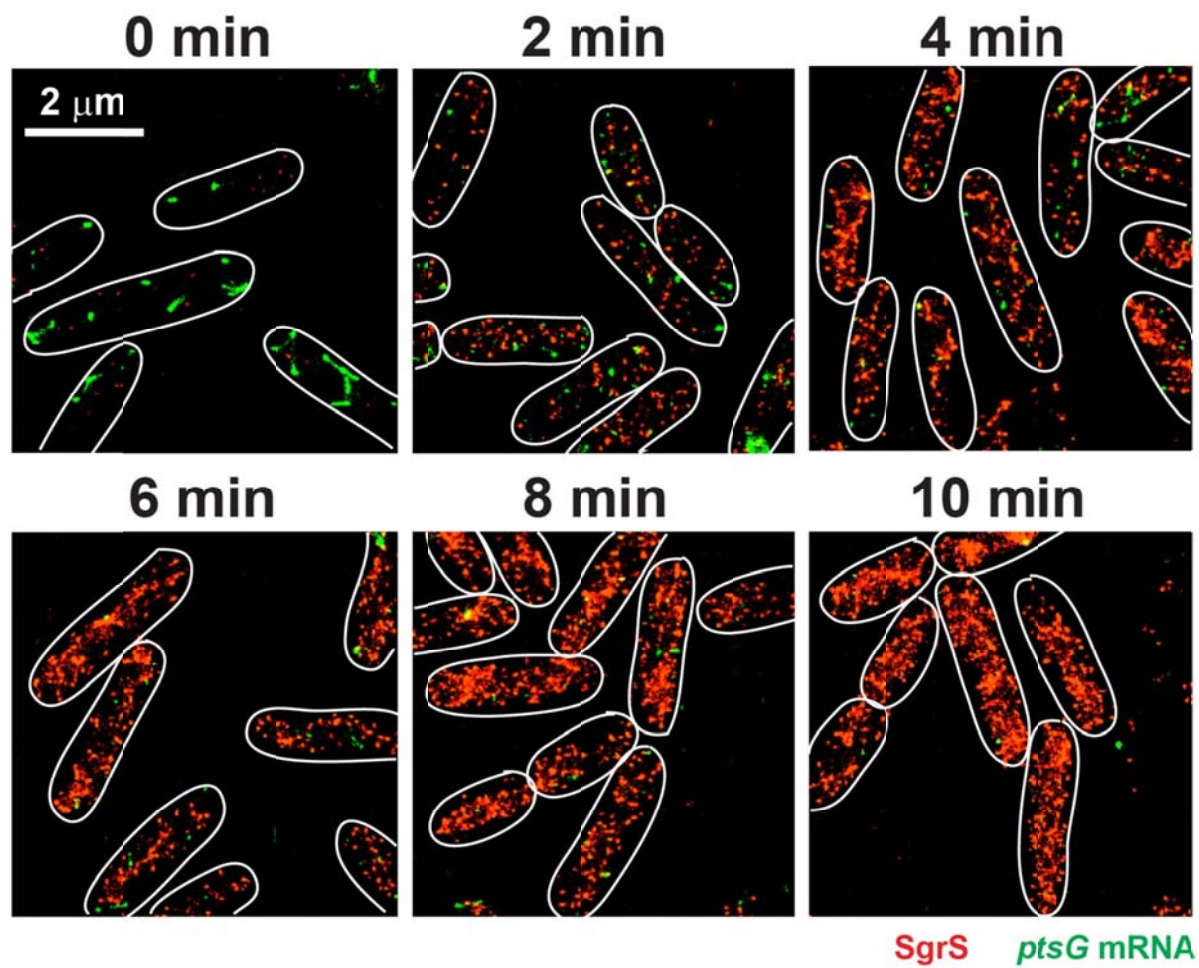


**Figure S7.** Time-dependent changes of SgrS (red) and *ptsG* mRNA (green) in the wild-type strain in the absence of glucose in the growth medium. Description of the figure is the same as in Fig. 1A.

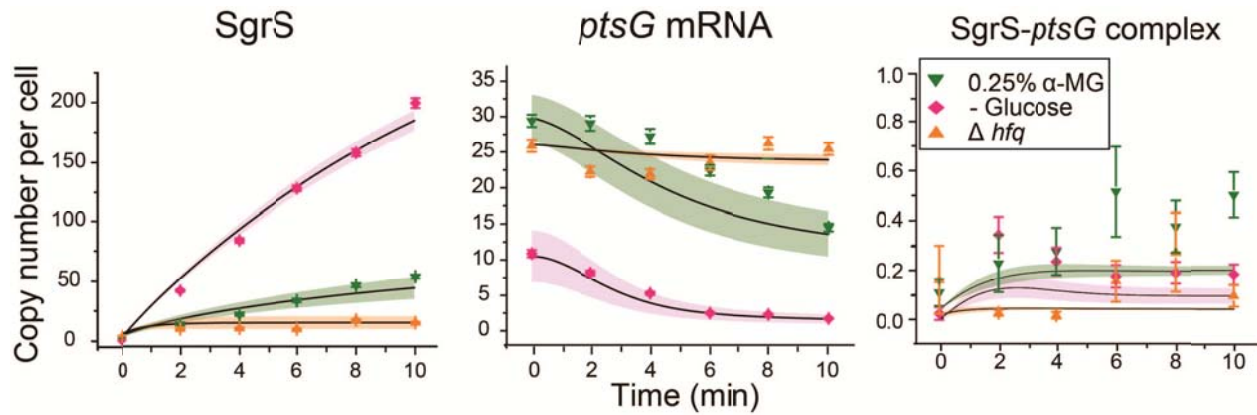


**Figure S8. Fitting of the time-course changes of SgrS, *ptsG* mRNA and SgrS-*ptsG* complex.** Average copy number of SgrS, *ptsG* mRNA and SgrS-*ptsG* complex per cell are plotted as a function of time. Error bars are standard errors from 200-600 cells from two independent measurements. Each measurement is fitted independently. The black curves and areas with corresponding colors reflect the mean and standard deviation from the fittings. Weighted  $R^2$  or  $\chi^2$  are reported in Table S5

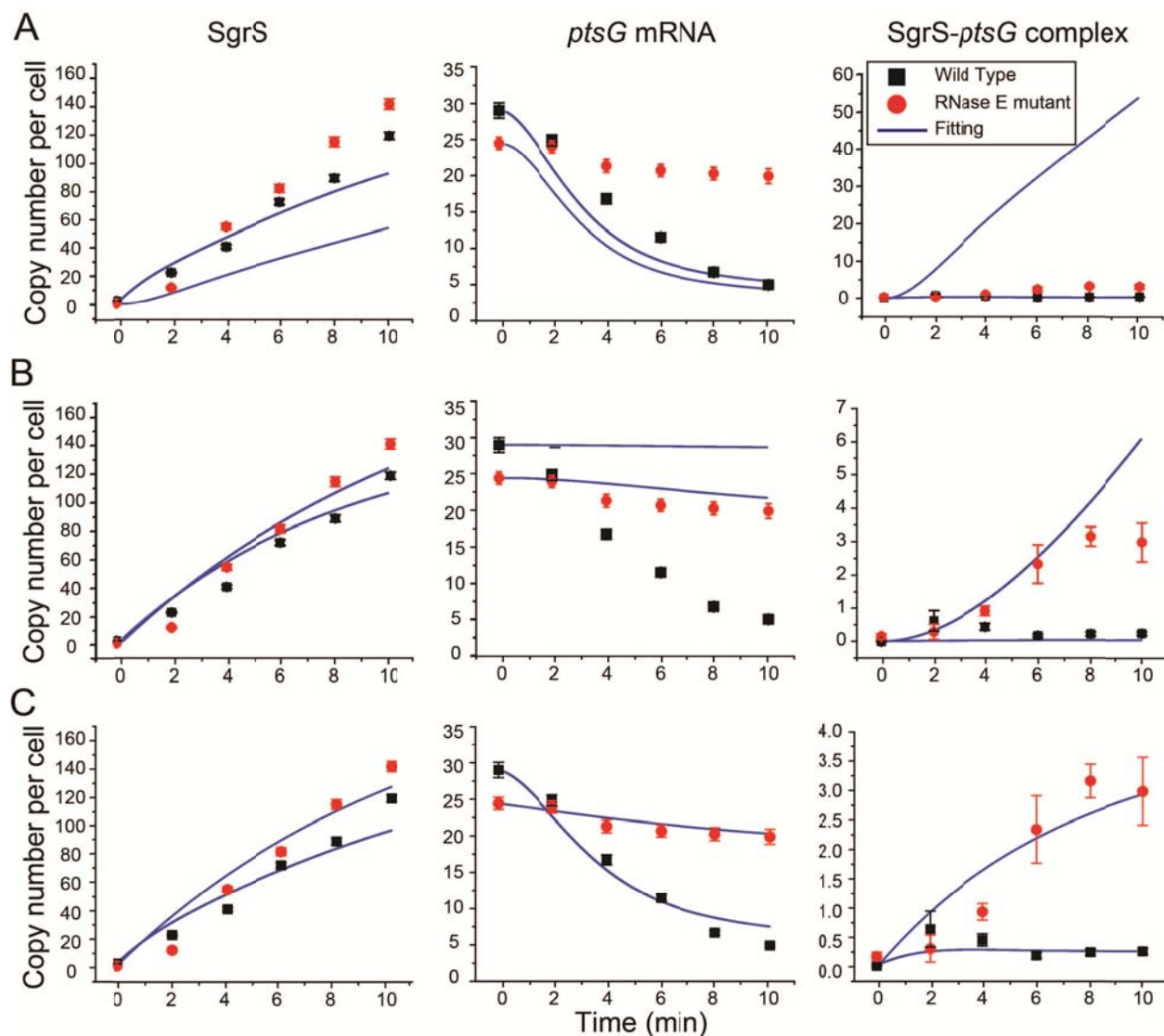


**Figure S9. Fitting of the time-course changes of SgrS, *ptsG* mRNA and the SgrS-*ptsG* complex in the cases of zero  $k_{off}$  and non-zero  $k_{cat}$  in the RNase E mutant strain.** Average copy number of SgrS and *ptsG* mRNA per cell are plotted as a function of time. Error bars are standard errors from 200-600 cells from two independent measurements. Fitting (blue curve) is performed using the average of two experimental data sets. (A)  $k_{off}$  is set to zero while other parameters remain the same as in the wild-type and RNase E mutant strains listed in Table S4. (B)  $k_{off}$  is set to zero while other parameters are determined by optimization of global  $R^2$ . (C)  $k_{cat}$  in the RNase E mutant is searched as a free parameter together with others instead of being set to zero. Rate constants are discussed in Section 2.1. Weighted  $R^2$  or  $\chi^2$  for the new parameter search in (B) and (C) are reported in Table S5.

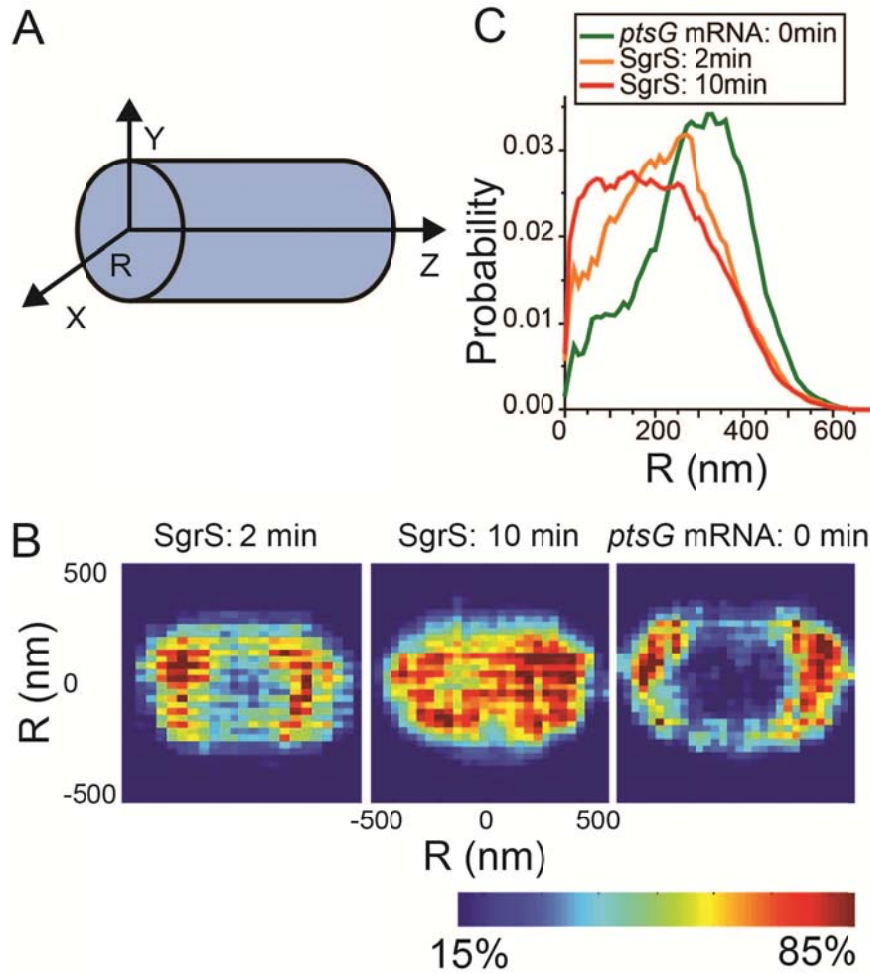


**Figure S10. Cellular distribution of *ptsG* mRNA and SgrS.** (A) The longitudinal axis of an *E. coli* cell is defined as the Z axis and the 2D cross section is defined as the XY plane. (B) Images of individual cells are projected along Z axis to generate heat map of radial distribution on the XY plane. (C) Probability distributions of SgrS and *ptsG* mRNA along the radius (R) of the cross section.

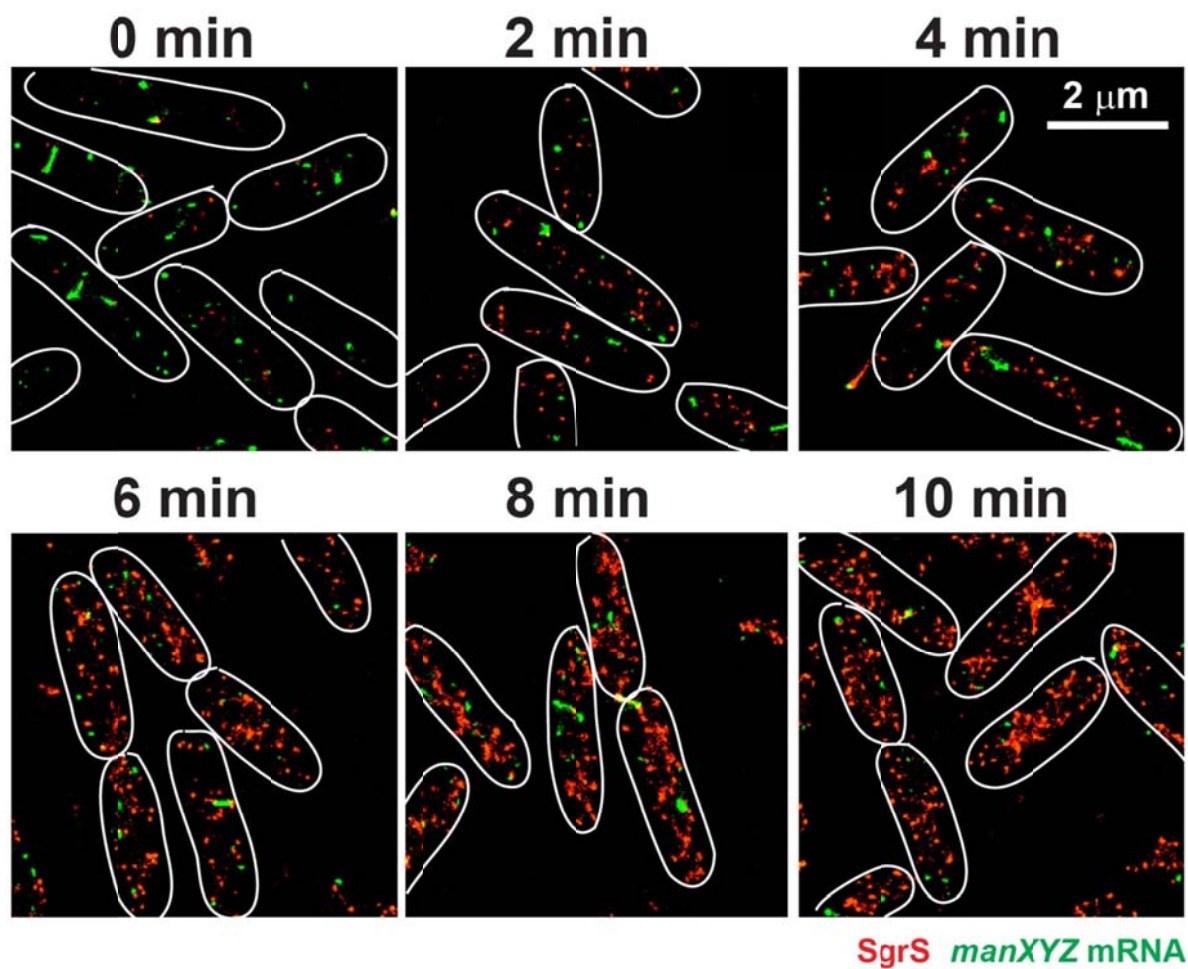


**Figure S11.** Time-dependent changes of SgrS (red) and *manXYZ* mRNA (green) in wild-type strain with glucose in the growth medium. Description of the figure is the same as in Fig. 1A.

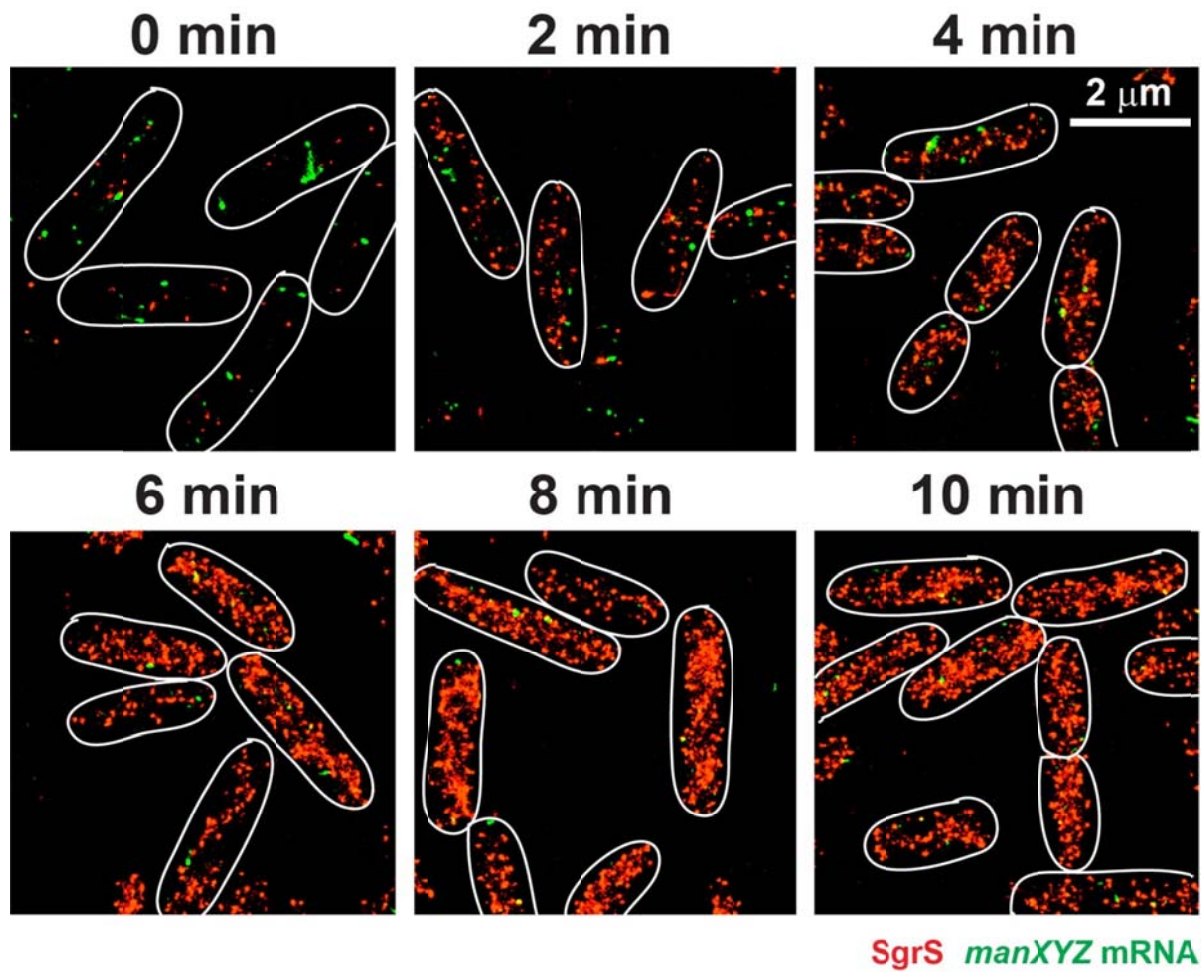


**Figure S12.** Time-dependent changes of SgrS (red) and *manXYZ* mRNA (green) in the wild-type strain without glucose in the growth medium. Description of the figure is the same as in Fig. 1A.

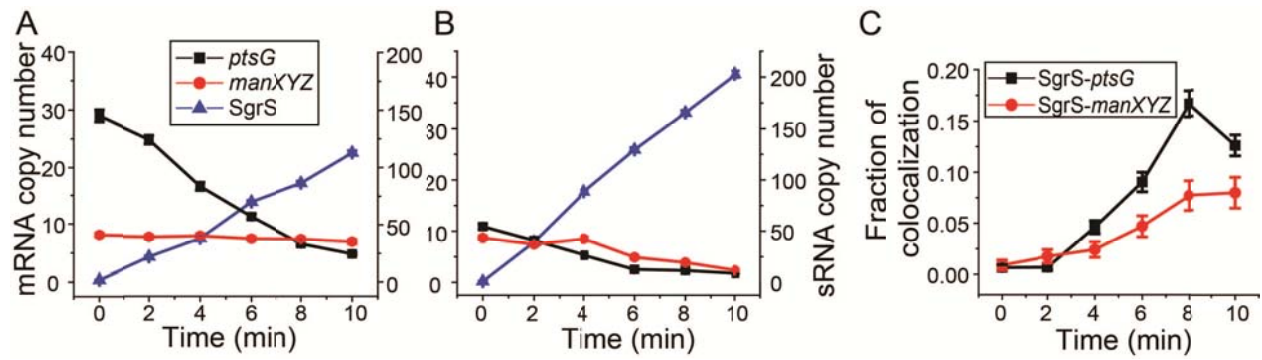


**Figure S13. Comparison of kinetics of SgrS regulation on *ptsG* and *manXYZ* mRNAs.** Cells are grown in the presence (A) and absence (B) of glucose. (C) Kinetics of SgrS-mRNA complex formation in the RNase E mutant strain in the presence of glucose. Error bars are standard errors from 200-600 cells from two independent measurements.

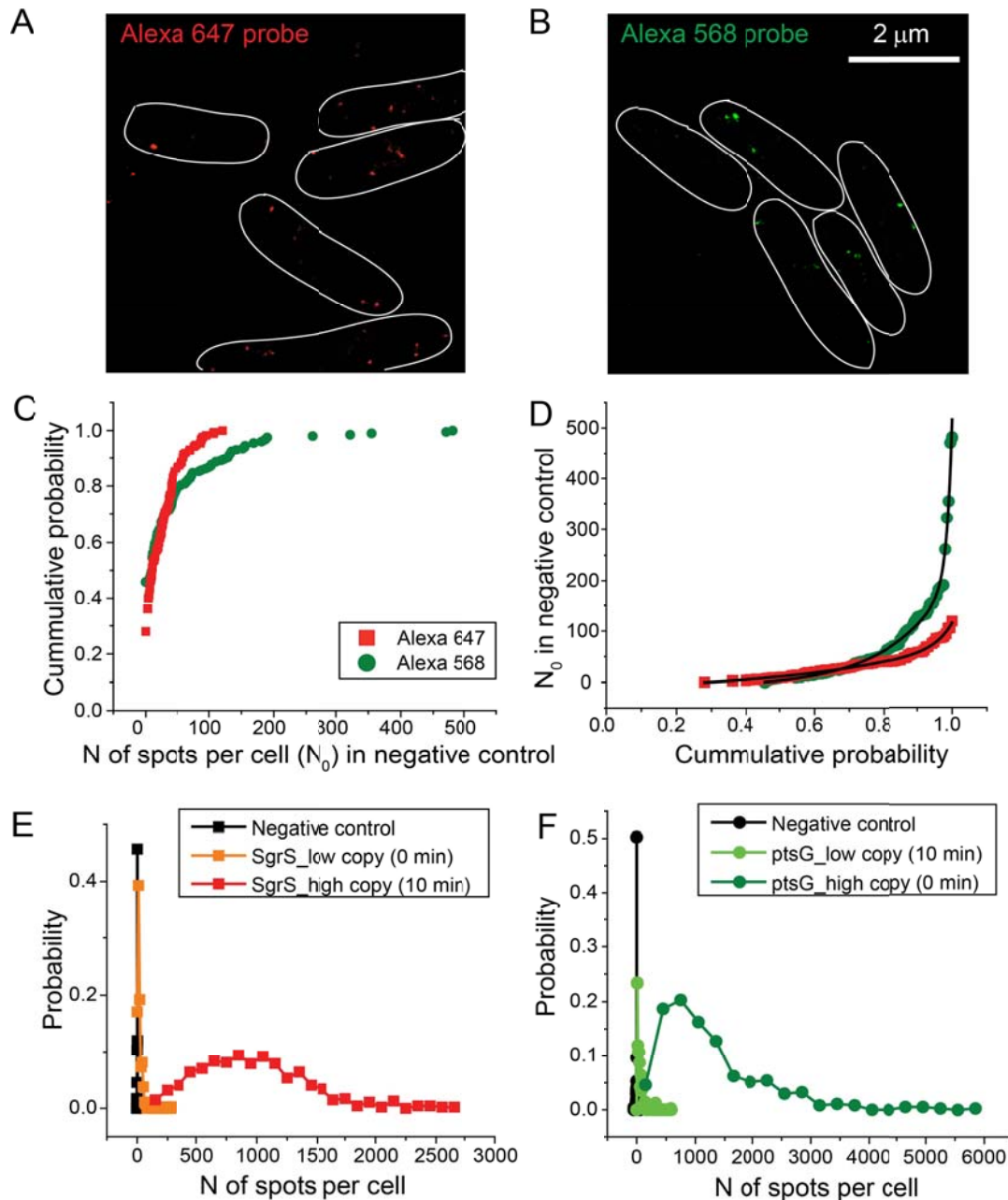


**Figure S14. Negative control and baseline correction for copy number calculation.** (A) Background due to non-specific binding of Alexa 647-labeled probes against SgrS in  $\Delta sgrS$  strain. (B) Background due to non-specific binding of Alexa 568-labeled probes against *ptsG* mRNA in  $\Delta ptsG$  strain. (C) Cumulative probability distribution of the number of spots per cell ( $N_0$ ) in the clustered data for (A) and (B). (D) Inversed cumulative probability distribution in (C) is fit with double-exponential growth. Distribution of the number of spots per cell after baseline correction for both low-copy number and high-copy number cases: (E) SgrS and (F) *ptsG* mRNA.

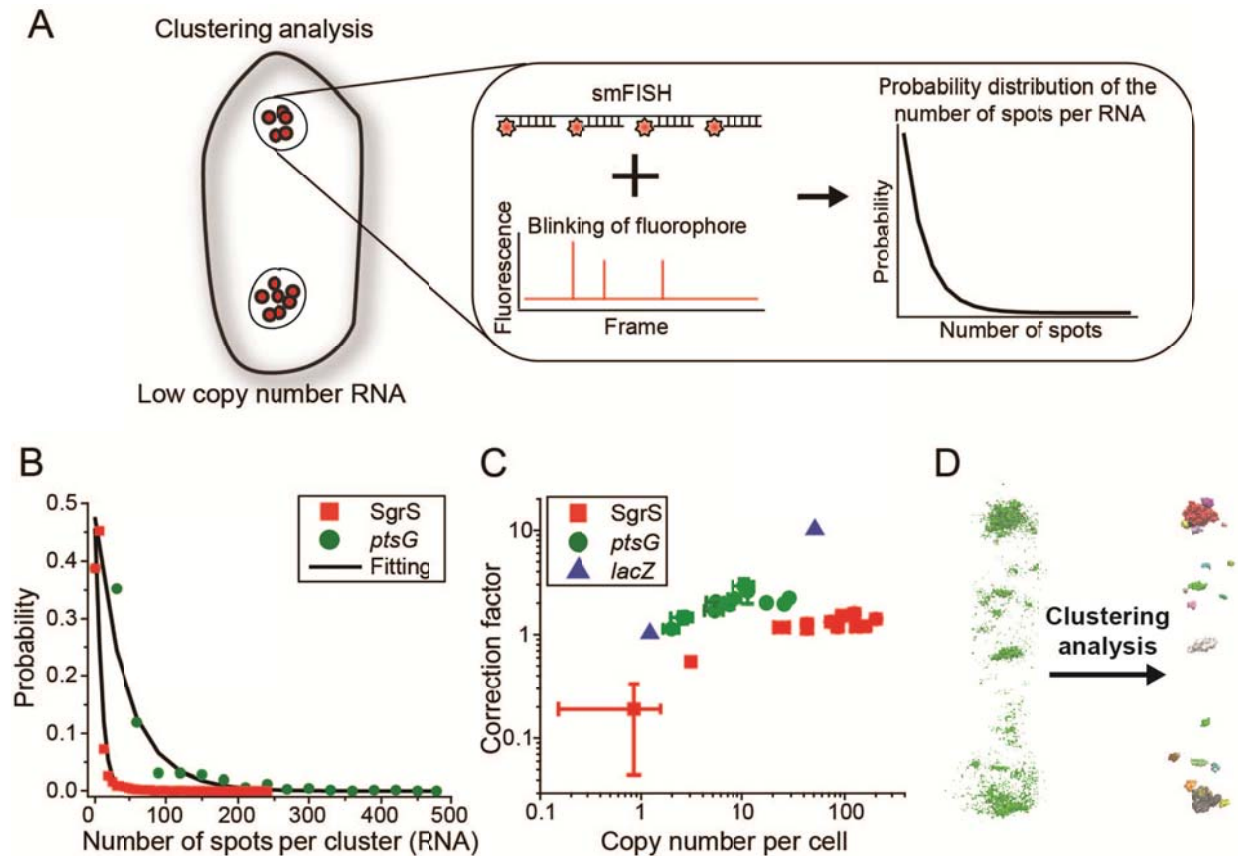


**Figure S15. Copy number calculation.** (A) Illustration of copy number calculation. Samples containing low copy number of RNA are used to estimate RNA copy number per cell. In low copy number case, individual clusters are approximated as individual RNAs. The heterogeneity in the number of spots per RNA (cluster) is contributed by both the heterogeneities of number of hybridized probes per RNA and the number of spots (blinking events) generated per fluorophore. The resulted distribution of the number of spots per RNA (cluster) is empirically described by negative binomial distribution (Section 1.6). (B) Probability distribution of the number of spots per cluster in very low-copy number case for SgrS and *ptsG* mRNA. The probability distributions are described with negative binomial distribution. (C) Correction factor, defined as the ratio of the average number of RNA per cell to the average number of cluster per cell, is plotted as a function of RNA copy number per cell. (D) Example of clustering analysis on *lacZ* mRNA.

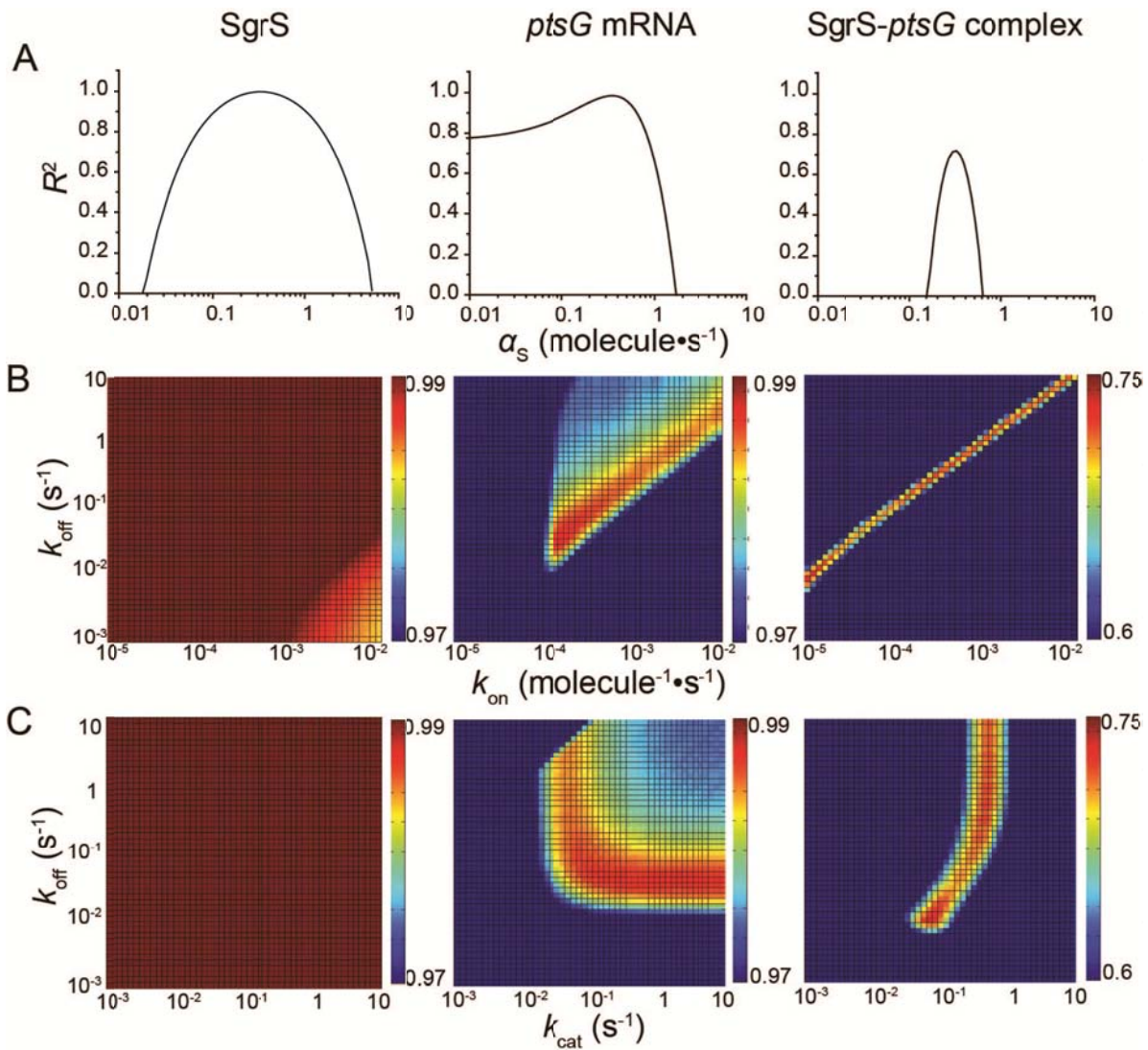


**Figure S16. Parameter dependence of  $R^2$  for modeling on SgrS, *ptsG* mRNA and SgrS-*ptsG* complex.** (A) Dependence of  $R^2$  on  $\alpha_s$ . (B) Dependence of  $R^2$  on the combination of  $k_{\text{on}}$  and  $k_{\text{off}}$ . (C) Dependence of  $R^2$  on the combination of  $k_{\text{cat}}$  and  $k_{\text{off}}$ .

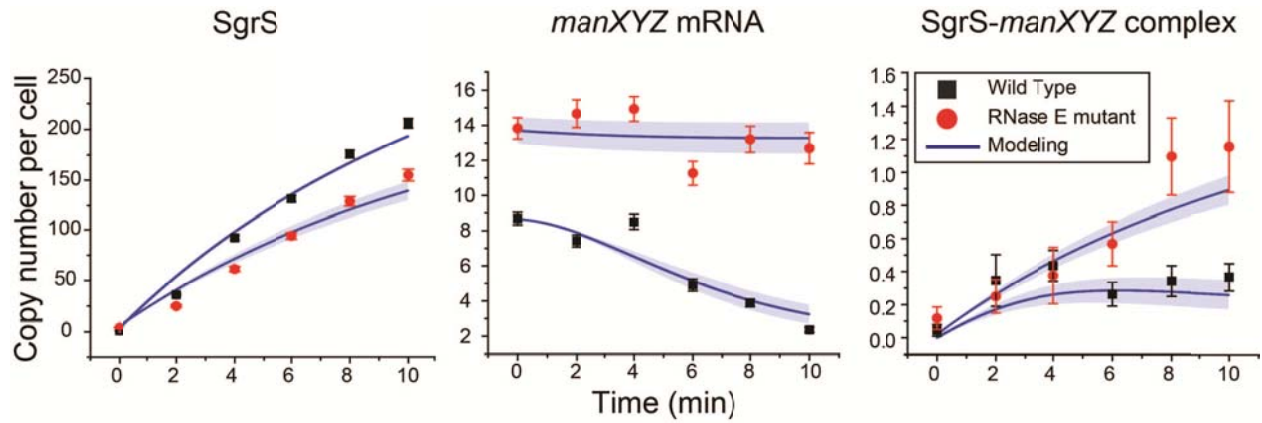


**Figure S17. Fitting of the time-course changes of SgrS and *manXYZ* mRNA.** Average copy number of SgrS and *manXYZ* mRNA per cell are plotted as a function of time. Error bars are standard errors from 200-600 cells from two independent measurements. Each measurement is fitted independently. The blue curves and areas with corresponding colors reflect the mean and standard deviation from the fittings. Weighted  $R^2$  or  $\chi^2$  are reported in Table S5.

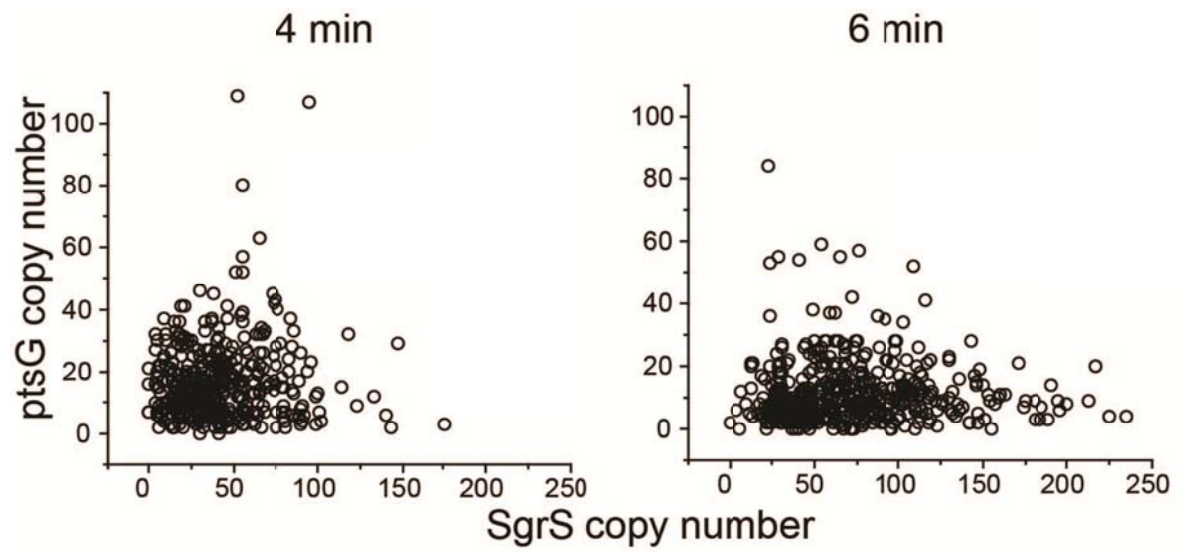


**Figure S18. Copy number of *ptsG* mRNA vs. *SgrS* for individual cells.** Data are combined from two measurements with 100-300 cells in each.

## Supplementary Movie Captions

**Video S1. Clustering analysis of SgrS.** 3D rotation of SgrS signal in one *E. coli* cell with (A) raw data and (B) analyzed data. Individual clusters in the clustered data are colored differently to distinguish in (B). Videos are rendered in VMD (54).

**Video S2. Clustering analysis of *ptsG* mRNA.** 3D rotation of *ptsG* mRNA signal in one *E. coli* cell with (A) raw data and (B) analyzed data. Individual clusters in the clustered data are colored differently to distinguish in (B). Videos are rendered in VMD (54).

**Video S3. Clustering analysis of *lacZ* mRNA.** 3D rotation of *lacZ* mRNA signal in one *E. coli* cell with (A) raw data and (B) analyzed data. Individual clusters in the clustered data are colored differently to distinguish in (B). Videos are rendered in VMD (54).

## References

1. A. M. Gurtan, P. A. Sharp, The role of miRNAs in regulating gene expression networks. *J. Mol. Biol.* **425**, 3582–3600 (2013). [Medline doi:10.1016/j.jmb.2013.03.007](#)
2. S. Geisler, J. Collier, RNA in unexpected places: Long non-coding RNA functions in diverse cellular contexts. *Nat. Rev. Mol. Cell Biol.* **14**, 699–712 (2013). [Medline doi:10.1038/nrm3679](#)
3. G. Storz, J. Vogel, K. M. Wassarman, Regulation by small RNAs in bacteria: Expanding frontiers. *Mol. Cell* **43**, 880–891 (2011). [Medline doi:10.1016/j.molcel.2011.08.022](#)
4. B. Wiedenheft, S. H. Sternberg, J. A. Doudna, RNA-guided genetic silencing systems in bacteria and archaea. *Nature* **482**, 331–338 (2012). [Medline doi:10.1038/nature10886](#)
5. A. Malkova, G. Ira, Break-induced replication: Functions and molecular mechanism. *Curr. Opin. Genet. Dev.* **23**, 271–279 (2013). [Medline doi:10.1016/j.gde.2013.05.007](#)
6. J. Elf, G. W. Li, X. S. Xie, Probing transcription factor dynamics at the single-molecule level in a living cell. *Science* **316**, 1191–1194 (2007). [Medline doi:10.1126/science.1141967](#)
7. M. Bobrovskyy, C. K. Vanderpool, Regulation of bacterial metabolism by small RNAs using diverse mechanisms. *Annu. Rev. Genet.* **47**, 209–232 (2013). [Medline doi:10.1146/annurev-genet-111212-133445](#)
8. A. Raj, P. van den Bogaard, S. A. Rifkin, A. van Oudenaarden, S. Tyagi, Imaging individual mRNA molecules using multiple singly labeled probes. *Nat. Methods* **5**, 877–879 (2008). [Medline doi:10.1038/nmeth.1253](#)
9. B. Huang, S. A. Jones, B. Brandenburg, X. Zhuang, Whole-cell 3D STORM reveals interactions between cellular structures with nanometer-scale resolution. *Nat. Methods* **5**, 1047–1052 (2008). [Medline doi:10.1038/nmeth.1274](#)
10. C. K. Vanderpool, S. Gottesman, Involvement of a novel transcriptional activator and small RNA in post-transcriptional regulation of the glucose phosphoenolpyruvate phosphotransferase system. *Mol. Microbiol.* **54**, 1076–1089 (2004). [Medline doi:10.1111/j.1365-2958.2004.04348.x](#)
11. K. Kimata, Y. Tanaka, T. Inada, H. Aiba, Expression of the glucose transporter gene, *ptsG*, is regulated at the mRNA degradation step in response to glycolytic flux in *Escherichia coli*. *EMBO J.* **20**, 3587–3595 (2001). [Medline doi:10.1093/emboj/20.13.3587](#)
12. Materials and methods are available as supplementary materials on *Science Online*.
13. H. Kawamoto, Y. Koide, T. Morita, H. Aiba, Base-pairing requirement for RNA silencing by a bacterial small RNA and acceleration of duplex formation by Hfq. *Mol. Microbiol.* **61**, 1013–1022 (2006). [Medline doi:10.1111/j.1365-2958.2006.05288.x](#)
14. C. S. Wadler, C. K. Vanderpool, Characterization of homologs of the small RNA SgrS reveals diversity in function. *Nucleic Acids Res.* **37**, 5477–5485 (2009). [Medline doi:10.1093/nar/gkp591](#)
15. M. Ester, H. Kriegel, J. Sander, X. Xu, in *Proceedings of the Second International Conference on Knowledge Discovery and Data Mining*, Portland, Oregon (Association for the Advancement of Artificial Intelligence, Palo Alto, CA, 1996), pp. 226–231.

16. M. Daszykowski, B. Walczak, D. L. Massart, Looking for natural patterns in data. Part 1: Density-based approach. *Chemom. Intell. Lab. Syst.* **56**, 83–92 (2001). [doi:10.1016/S0169-7439\(01\)00111-3](https://doi.org/10.1016/S0169-7439(01)00111-3)
17. T. Morita, H. Kawamoto, T. Mizota, T. Inada, H. Aiba, Enolase in the RNA degradosome plays a crucial role in the rapid decay of glucose transporter mRNA in the response to phosphosugar stress in *Escherichia coli*. *Mol. Microbiol.* **54**, 1063–1075 (2004). [Medline doi:10.1111/j.1365-2958.2004.04329.x](https://pubmed.ncbi.nlm.nih.gov/15111111/)
18. T. Morita, K. Maki, H. Aiba, RNase E-based ribonucleoprotein complexes: Mechanical basis of mRNA destabilization mediated by bacterial noncoding RNAs. *Genes Dev.* **19**, 2176–2186 (2005). [Medline doi:10.1101/gad.1330405](https://pubmed.ncbi.nlm.nih.gov/15110101/)
19. E. Lubeck, L. Cai, Single-cell systems biology by super-resolution imaging and combinatorial labeling. *Nat. Methods* **9**, 743–748 (2012). [Medline doi:10.1038/nmeth.2069](https://pubmed.ncbi.nlm.nih.gov/22069/)
20. J. Vogel, B. F. Luisi, Hfq and its constellation of RNA. *Nat. Rev. Microbiol.* **9**, 578–589 (2011). [Medline doi:10.1038/nrmicro2615](https://pubmed.ncbi.nlm.nih.gov/22615/)
21. V. Arluison, S. Hohng, R. Roy, O. Pellegrini, P. Régnier, T. Ha, Spectroscopic observation of RNA chaperone activities of Hfq in post-transcriptional regulation by a small non-coding RNA. *Nucleic Acids Res.* **35**, 999–1006 (2007). [Medline doi:10.1093/nar/gkl1124](https://pubmed.ncbi.nlm.nih.gov/171124/)
22. W. Hwang, V. Arluison, S. Hohng, Dynamic competition of DsrA and *rpoS* fragments for the proximal binding site of Hfq as a means for efficient annealing. *Nucleic Acids Res.* **39**, 5131–5139 (2011). [Medline doi:10.1093/nar/gkr075](https://pubmed.ncbi.nlm.nih.gov/21075/)
23. T. J. Soper, S. A. Woodson, The *rpoS* mRNA leader recruits Hfq to facilitate annealing with DsrA sRNA. *RNA* **14**, 1907–1917 (2008). [Medline doi:10.1261/rna.1110608](https://pubmed.ncbi.nlm.nih.gov/1810608/)
24. A. Fender, J. Elf, K. Hampel, B. Zimmermann, E. G. Wagner, RNAs actively cycle on the Sm-like protein Hfq. *Genes Dev.* **24**, 2621–2626 (2010). [Medline doi:10.1101/gad.591310](https://pubmed.ncbi.nlm.nih.gov/201310/)
25. R. Hussein, H. N. Lim, Disruption of small RNA signaling caused by competition for Hfq. *Proc. Natl. Acad. Sci. U.S.A.* **108**, 1110–1115 (2011). [Medline doi:10.1073/pnas.1010082108](https://pubmed.ncbi.nlm.nih.gov/21082108/)
26. E. Levine, Z. Zhang, T. Kuhlman, T. Hwa, Quantitative characteristics of gene regulation by small RNA. *PLOS Biol.* **5**, e229 (2007). [Medline doi:10.1371/journal.pbio.0050229](https://pubmed.ncbi.nlm.nih.gov/180229/)
27. D. Jost, A. Nowojewski, E. Levine, Regulating the many to benefit the few: Role of weak small RNA targets. *Biophys. J.* **104**, 1773–1782 (2013). [Medline doi:10.1016/j.bpj.2013.02.020](https://pubmed.ncbi.nlm.nih.gov/24020/)
28. J. B. Rice, C. K. Vanderpool, The small RNA SgrS controls sugar-phosphate accumulation by regulating multiple PTS genes. *Nucleic Acids Res.* **39**, 3806–3819 (2011). [Medline doi:10.1093/nar/gkq1219](https://pubmed.ncbi.nlm.nih.gov/21219/)
29. Y. Sun, C. K. Vanderpool, Physiological consequences of multiple-target regulation by the small RNA SgrS in *Escherichia coli*. *J. Bacteriol.* **195**, 4804–4815 (2013). [Medline doi:10.1128/JB.00722-13](https://pubmed.ncbi.nlm.nih.gov/2422-13/)

30. K. A. Datsenko, B. L. Wanner, One-step inactivation of chromosomal genes in *Escherichia coli* K-12 using PCR products. *Proc. Natl. Acad. Sci. U.S.A.* **97**, 6640–6645 (2000). [Medline doi:10.1073/pnas.120163297](#)
31. L. H. So, A. Ghosh, C. Zong, L. A. Sepúlveda, R. Segev, I. Golding, General properties of transcriptional time series in *Escherichia coli*. *Nat. Genet.* **43**, 554–560 (2011). [Medline doi:10.1038/ng.821](#)
32. M. Swoboda, J. Henig, H. M. Cheng, D. Brugger, D. Haltrich, N. Plumere, M. Schlierf, Enzymatic oxygen scavenging for photostability without pH drop in single-molecule experiments. *ACS Nano* **6**, 6364–6369 (2012). [doi:10.1021/nn301895c](#) [Medline](#)
33. B. Huang, W. Wang, M. Bates, X. Zhuang, Three-dimensional super-resolution imaging by stochastic optical reconstruction microscopy. *Science* **319**, 810–813 (2008). [Medline doi:10.1126/science.1153529](#)
34. C. C. Fu, H. Y. Lee, K. Chen, T. S. Lim, H. Y. Wu, P. K. Lin, P. K. Wei, P. H. Tsao, H. C. Chang, W. Fann, Characterization and application of single fluorescent nanodiamonds as cellular biomarkers. *Proc. Natl. Acad. Sci. U.S.A.* **104**, 727–732 (2007). [Medline doi:10.1073/pnas.0605409104](#)
35. M. J. Rust, M. Bates, X. Zhuang, Sub-diffraction-limit imaging by stochastic optical reconstruction microscopy (STORM). *Nat. Methods* **3**, 793–796 (2006). [Medline doi:10.1038/nmeth929](#)
36. U. Alon, *An Introduction to Systems Biology: Design Principles of Biological Circuits* (Chapman & Hall/CRC, London, 2006).
37. S. Altuvia, D. Weinstein-Fischer, A. Zhang, L. Postow, G. Storz, A small, stable RNA induced by oxidative stress: Role as a pleiotropic regulator and antimutator. *Cell* **90**, 43–53 (1997). [Medline doi:10.1016/S0092-8674\(00\)80312-8](#)
38. E. Levine, Z. Zhang, T. Kuhlman, T. Hwa, Quantitative characteristics of gene regulation by small RNA. *PLOS Biol.* **5**, e229 (2007). [Medline doi:10.1371/journal.pbio.0050229](#)
39. Y. Shimoni, G. Friedlander, G. Hetzroni, G. Niv, S. Altuvia, O. Biham, H. Margalit, Regulation of gene expression by small non-coding RNAs: A quantitative view. *Mol. Syst. Biol.* **3**, 138 (2007). [Medline doi:10.1038/msb4100181](#)
40. D. Jost, A. Nowojewski, E. Levine, Regulating the many to benefit the few: Role of weak small RNA targets. *Biophys. J.* **104**, 1773–1782 (2013). [Medline doi:10.1016/j.bpj.2013.02.020](#)
41. J. B. Rice, D. Balasubramanian, C. K. Vanderpool, Small RNA binding-site multiplicity involved in translational regulation of a polycistronic mRNA. *Proc. Natl. Acad. Sci. U.S.A.* **109**, E2691–E2698 (2012). [Medline doi:10.1073/pnas.1207927109](#)
42. K. Kimata, H. Takahashi, T. Inada, P. Postma, H. Aiba, cAMP receptor protein-cAMP plays a crucial role in glucose-lactose diauxie by activating the major glucose transporter gene in *Escherichia coli*. *Proc. Natl. Acad. Sci. U.S.A.* **94**, 12914–12919 (1997). [Medline doi:10.1073/pnas.94.24.12914](#)

43. K. Kimata, T. Inada, H. Tagami, H. Aiba, A global repressor (Mlc) is involved in glucose induction of the *ptsG* gene encoding major glucose transporter in *Escherichia coli*. *Mol. Microbiol.* **29**, 1509–1519 (1998). [Medline doi:10.1046/j.1365-2958.1998.01035.x](#)
44. H. Hagihira, T. H. Wilson, E. C. Lin, Studies on the glucose-transport system in *Escherichia coli* with alpha-methylglucoside as substrate. *Biochim. Biophys. Acta* **78**, 505–515 (1963). [Medline doi:10.1016/0006-3002\(63\)90912-0](#)
45. P. W. Postma, J. W. Lengeler, G. R. Jacobson, Phosphoenolpyruvate:carbohydrate phosphotransferase systems of bacteria. *Microbiol. Rev.* **57**, 543–594 (1993). [Medline](#)
46. R. G. Brennan, T. M. Link, Hfq structure, function and ligand binding. *Curr. Opin. Microbiol.* **10**, 125–133 (2007). [Medline doi:10.1016/j.mib.2007.03.015](#)
47. D. Balasubramanian, C. K. Vanderpool, Deciphering the interplay between two independent functions of the small RNA regulator SgrS in Salmonella. *J. Bacteriol.* **195**, 4620–4630 (2013). [Medline doi:10.1128/JB.00586-13](#)
48. C. S. Wadler, C. K. Vanderpool, A dual function for a bacterial small RNA: SgrS performs base pairing-dependent regulation and encodes a functional polypeptide. *Proc. Natl. Acad. Sci. U.S.A.* **104**, 20454–20459 (2007). [Medline doi:10.1073/pnas.0708102104](#)
49. R. L. Gourse, T. Gaal, M. S. Bartlett, J. A. Appleman, W. Ross, rRNA transcription and growth rate-dependent regulation of ribosome synthesis in *Escherichia coli*. *Annu. Rev. Microbiol.* **50**, 645–677 (1996). [Medline doi:10.1146/annurev.micro.50.1.645](#)
50. J. Elf, J. Paulsson, O. G. Berg, M. Ehrenberg, Near-critical phenomena in intracellular metabolite pools. *Biophys. J.* **84**, 154–170 (2003). [Medline doi:10.1016/S0006-3495\(03\)74839-5](#)
51. Y. Ikeda, M. Yagi, T. Morita, H. Aiba, Hfq binding at RhlB-recognition region of RNase E is crucial for the rapid degradation of target mRNAs mediated by sRNAs in *Escherichia coli*. *Mol. Microbiol.* **79**, 419–432 (2011). [Medline doi:10.1111/j.1365-2958.2010.07454.x](#)
52. A. Miczak, V. R. Kaberdin, C. L. Wei, S. Lin-Chao, Proteins associated with RNase E in a multicomponent ribonucleolytic complex. *Proc. Natl. Acad. Sci. U.S.A.* **93**, 3865–3869 (1996). [Medline doi:10.1073/pnas.93.9.3865](#)
53. T. Kuhlman, Z. Zhang, M. H. Saier Jr., T. Hwa, Combinatorial transcriptional control of the lactose operon of *Escherichia coli*. *Proc. Natl. Acad. Sci. U.S.A.* **104**, 6043–6048 (2007). [Medline doi:10.1073/pnas.0606717104](#)
54. W. Humphrey, A. Dalke, K. Schulten, VMD: Visual molecular dynamics. *J. Mol. Graph.* **14**, 33–38, 27–28 (1996). [Medline doi:10.1016/0263-7855\(96\)00018-5](#)